Journal of Computational Physics 483 (2023) 112056

Contents lists available at ScienceDirect

Journal of Computational Physics

journal homepage: www.elsevier.com/locate/jcp

Inclusion of an acoustic damper term in weakly-compressible SPH models

P.N. Sun [a], C. Pilloton [b], M. Antuono [b,*], A. Colagrossi [b]

[a] School of Ocean Engineering and Technology, Sun Yat-sen University, Zhuhai, 519000, China
[b] CNR-INM, Institute of Marine Engineering, Rome, 00128, Italy

ARTICLE INFO

Article history:
Received 17 August 2022
Received in revised form 18 January 2023
Accepted 3 March 2023
Available online 16 March 2023

Keywords:
Smoothed particle hydrodynamics
Acoustic damper
Water impact flows
Delta-SPH
Delta-Plus-SPH

ABSTRACT

The proposed work describes a novel viscous term specifically conceived to reduce the amount of acoustic pressure waves in weakly-compressible SPH models. The above-mentioned term only acts on the acoustic component of the pressure field, which is generated as a consequence of liquid impacts and of the assumption that the fluid is weakly-compressible, whereas it leaves the incompressible-like component unchanged. In comparison to the existing regularizing terms in the SPH literature, this allows for noise-free simulations which are similar to simulations of incompressible flows, and, at the same time, it maintains the advantages of explicit schemes (*i.e.* scalability and easiness of parallelization). The proposed acoustic damper term converges to zero when the particle resolution increases, recovering the consistency with the Navier-Stokes equations. Numerical results demonstrate that this term is effective for flow simulations with different weakly-compressible SPH models.

1. Introduction

In the last decade the SPH model has been widely applied to simulate free-surface flows and water wave impacts (see *e.g.* [11,62,26–28,75,18,40]) and, more recently, in complex solid dynamics (see *e.g.* [81,23,76]) and multi-physics problems (see *e.g.* [78,79]). The SPH schemes can be mainly divided into two categories, incompressible SPH variants with pressure field solved by a pressure Poisson equation (see *e.g.* [38,35,30,77,80]) and weakly-compressible SPH variants defined through the use of a reduced sound speed in comparison to the actual one.

The latter approach allows for the definition of schemes that are explicit in time and avoids the solution of large linear systems associated with the Poisson equation. For this reason, weakly-compressible SPH models are widely employed thanks to their simple structure and the easier code parallelization, and large scale simulations can be launched in industrial applications by using multi-CPU or multi-GPU systems (see *e.g.* [86,84,62,85]). On the other hand, in hydrodynamics problems the weakly-compressibility assumption is used as an approximation for the modelling of incompressible fluids and, consequently, the effects related to the fluid compressibility are required to be as small as possible (see, for example, [41]). Different from the incompressible variants, the main drawback of the weakly-compressible SPH schemes is, in fact, the presence of acoustic waves. Although different pressure stabilization techniques are often implemented in weakly-compressible

* Corresponding author.
E-mail address: matteo.antuono@cnr.it (M. Antuono).

https://doi.org/10.1016/j.jcp.2023.112056
0021-9991/

SPH models (see *e.g.* density filters [15], diffusive terms [2,22] and Riemann solvers [71,33,57]), acoustic waves are still observed in flows with violent liquid-liquid or liquid-solid impacts.

In particular, in the simulations of violent fluid-solid interactions, strong liquid impacts on the structure generate a group of pressure waves (see *e.g.* [25,67,68]) whose reflection at the boundaries of the fluid domain causes nonphysical loads to the structure. To prevent the pressure reflection at the boundaries, non-reflecting boundary conditions were proposed (see *e.g.* [82,83]), but this approach just partially mitigates the presence of acoustic waves. Other problems where large pressure oscillations are induced in the flow are, for example, sloshing motions with periodical free-surface impacts on solid walls (see *e.g.* [49]). It is possible to show that the solution of a weakly-compressible fluid can be decomposed in an "incompressible-flow" component and an acoustic part which are superimposed in a complex and non-linear way. Unfortunately, it is not possible to filter out the acoustic component in a straightforward way and, for this reason, a post-processing filtering procedure is proposed in some works (see, for example, [49]). In fact, techniques like the density filters, diffusive terms and Riemann solvers are essentially proposed to prevent high-frequency pressure oscillations and they are mainly effective at length scales comparable to the kernel radius. On the contrary, the pressure waves generated by the reduced sound speeds are characterized by a larger scale and lower frequency and, consequently, they are only partially prevented by the existing techniques.

The aim of the present work is, then, to define a novel diffusive term specifically conceived to damp such acoustic oscillations. The basic idea is borrowed from the work of [7] where an appropriate dissipation function that depends on the rate of change of particle volume is introduced. The latter approach leads to the appearance of an "acoustic damper" term on the right-hand side of the momentum equation that preserves both linear and angular momenta and that is purely dissipative (namely, it gives a negatively-defined contribution to the energy balance). Some preliminary and partial results were described in [69] whereas an exhaustive and thorough analysis is proposed in the present work.

Thanks to its simple structure, the proposed "acoustic damper" term can be implemented in a generic weakly-compressible SPH model straightforwardly. In the present work we mostly use the δ^+-SPH scheme defined in [64], since the latter represents the most recent and promising advancement of the δ-SPH model. Then, in the last part of the paper we show some applications to different weakly-compressible SPH models.

The present work is structured as follows:

i) in Section §2 we provide a discussion on the decomposition of the weakly-compressible Navier-Stokes equations (NSEs) in two components, one related to the incompressible flow and the other linked to the acoustic-wave components;
ii) in Section §3 we introduce the δ^+-SPH scheme and describe the proposed acoustic damper term;
iii) Sections §3.2 and §3.3 clarify some details about the integration scheme and the conservation of energy;
iv) Section §4 shows the results of four different test-cases obtained by using the acoustic damper term in the δ^+-SPH scheme;
v) Section §5 describes outputs and comparisons for benchmarks obtained by using different weakly-compressible SPH models.

2. Navier-Stokes equations for weakly-compressible fluids

In a Lagrangian formalism the governing equations for a generic weakly-compressible barotropic fluid are:

$$\begin{cases} \dfrac{D\rho}{Dt} + \rho\,\nabla\cdot\boldsymbol{u} = 0\,, & \dfrac{D\boldsymbol{u}}{Dt} = \boldsymbol{g} - \dfrac{\nabla p}{\rho} + \dfrac{\nabla\cdot\mathbb{V}}{\rho}\,, \\ \dfrac{D\boldsymbol{r}}{Dt} = \boldsymbol{u}\,, & p = c_0^2\,(\rho-\rho_0)\,, \end{cases} \tag{1}$$

where ρ is the fluid density, p the pressure, c_0 the reference sound velocity and $\boldsymbol{g}$ is the external volume force. The flow velocity $\boldsymbol{u}$ is defined as the material derivative of a fluid element at the position $\boldsymbol{r}$. Since the variations of the density field are supposed to be small, the state equation is linearized around a reference density value, ρ_0, which generally refers to the density along the free surface. The weakly-compressible regime arises when the following condition is fulfilled:

$$c_0 \geq \max\left(10U_{max}\,,\,10\sqrt{(\Delta p)_{max}/\rho}\right), \tag{2}$$

where U_{max} and $(\Delta p)_{max}$ are respectively the maximum fluid speed and the maximum pressure variation (with respect to the pressure on the free-surface) expected in the fluid domain (see *e.g.* [46]). To avoid the occurrence of small time steps in numerical simulations, a numerical sound speed is generally chosen in SPH instead of the real physical value of c_0. Such a numerical sound speed has to satisfy, in any case, the constraint in the equation (2) during the simulations. This implies that the Mach number of the numerical scheme, *i.e.* $Ma = U_{max}/c_0$, satisfies $M_a \leq 0.1$.

In Eq. (1) $\mathbb{V}$ is the viscous stress tensor of a Newtonian fluid:

$$\mathbb{V} = \lambda\,\mathrm{tr}\,\mathbb{D}\,\mathbb{I} + 2\,\mu\,\mathbb{D}\,, \tag{3}$$

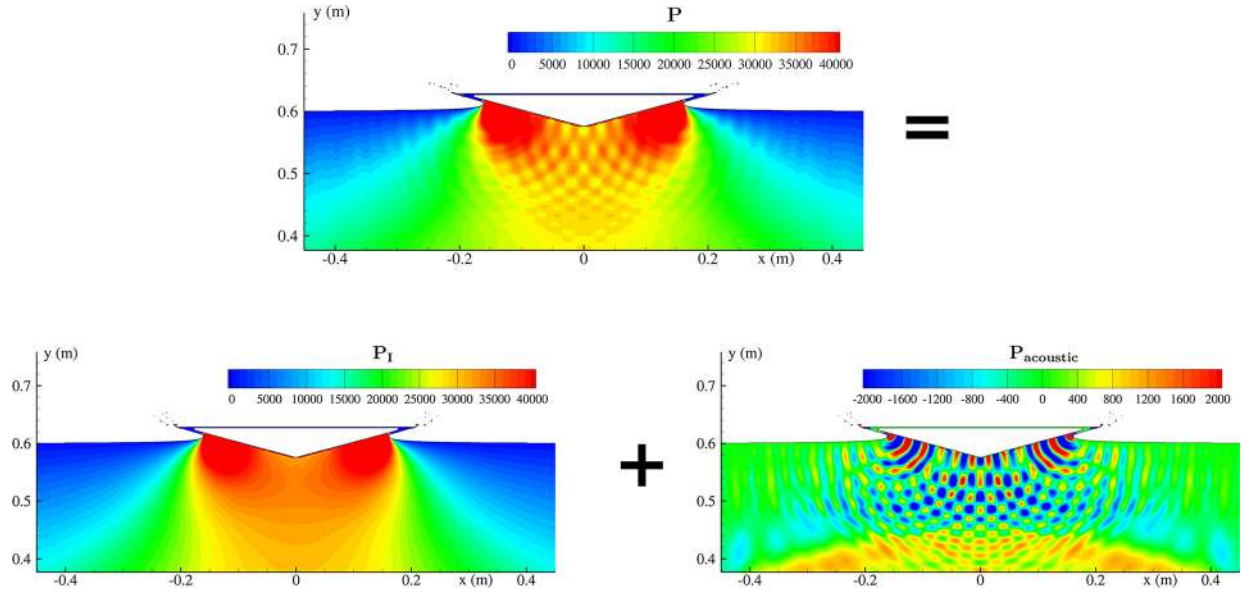

Fig. 1. Wedge entry problem. Top: Pressure solution at time $t = 0.008$ s using the wcNSEs (see Eq. (1)). Bottom: decomposition of the above pressure field as solution of the incompressible NSEs (left) and the acoustic component (right). (For interpretation of the colours in the figure(s), the reader is referred to the web version of this article.)

where $\mathbb{D}$ represents the rate of strain tensor, *i.e.* $\mathbb{D} = (\nabla \boldsymbol{u} + \nabla \boldsymbol{u}^T)/2$, while μ and λ are the Lamé constants where μ is the dynamic viscosity and λ the second viscosity. The viscous forces are given by the divergence of the viscous stress tensor, namely:

$$\begin{cases} \nabla \cdot \mathbb{V} = \boldsymbol{F}^v + \boldsymbol{F}^{ad}, \\ \boldsymbol{F}^v = \mu \left[\nabla^2 \boldsymbol{u} + \nabla(\nabla \cdot \boldsymbol{u}) \right], \qquad \boldsymbol{F}^{ad} = \lambda \nabla(\nabla \cdot \boldsymbol{u}). \end{cases} \tag{4}$$

Here the components of the viscous forces are split according to their dependence on μ and λ, since they are modelled in two different ways within the SPH framework (see section 3.1).

The above "weakly-compressible" framework is classically adopted in SPH formulations to model free-surface flows for which the compressibility is actually negligible. This choice is motivated by the possibility of employing a fully explicit method for the time integration (unlike solvers for incompressible fluids) and by the implicit fulfilment of both the kinematic and dynamic boundary conditions at the free surface (see [13]).

In simulations involving liquid/liquid or liquid/solid collisions, the fluid incompressibility can lead to instantaneous losses in the mechanical energy. On the contrary, when a liquid is modelled as a weakly-compressible fluid, part of the mechanical energy is converted into acoustic waves during the impacts. The energy associated with these waves is the energy due to the fluid compressibility and can be regarded as a sort of elastic energy. This part is generally dissipated by viscous effects only after several oscillation cycles, during which the elastic energy is transformed into mechanical energy and vice-versa.

In the limit of Mach number tending to zero (see [56,61]), the pressure P given by the solution of the wcNSEs (1) can be decomposed as $P = P_I + P_{acoustic}$, where P_I is the pressure solution of the incompressible NSEs and $P_{acoustic}$ is the acoustic pressure obtained by the D'Alembert wave equation, related to the non-null divergence component of the velocity field. As remarked in [16], in free-surface problems the displacement of the air-water interface is practically unaffected by the component $P_{acoustic}$.

An example of this decomposition is given in Fig. 1 for the water entry problem of a wedge with a deadrise angle of 15°. The wedge is freely dropped from height h = 0.75 m. When the wedge impacts against the water surface, its velocity is -3.834 m/s (see the experimental work of [73]). The top plot of Fig. 1 displays the pressure field obtained by solving the wcNSEs (1) with an artificial speed of sound $c_0 = 25$ m/s (that is two orders of magnitude less than the real one and about one order of magnitude larger than the velocity at the impact). The bottom plots of the same figure show the decomposition of the two components of the pressure: on the left the pressure given by the incompressible NSEs, P_I, and on the right the acoustic components $P_{acoustic}$.

Since the speed of sound c_0 is not the physical one, the acoustic pressure $P_{acoustic}$ is an unwanted output of the simulations, and it can be generally removed by the time series outputs of SPH simulations through filtering procedures, as discussed, for example, in [49].

We underline that the above decomposition is related to the adopted governing equations and not to the specific numerical schemes at hand (meshless or not). The solution of the wcNSEs through the different SPH variants available in literature can only improve the solution of the total pressure field P but does not eliminate the presence of the acoustic component.

The main idea of the present work is to demonstrate that the second viscosity force $\boldsymbol{F}^{ad}$ in Eq. (4) can be numerically increased in order to damp the unwanted acoustic waves generated within the weakly-compressible framework. The proposed technique represents a great benefit since it avoids the filtering procedure during the post-processing stages and, more importantly, it can drastically reduce the pressure acoustic component $P_{acoustic}$ in the whole fluid domain during the whole time evolution.

The use of the second viscosity as an artificial damping term is not new in the literature. For example the classical Von Neumann-Richtmyer artificial viscous pressure [72] is based on the spatial gradient of the velocity divergence and on the spatial gradient of the square of the velocity divergence. This kind of correction was used to stabilize schemes for highly compressible flows in the neighbourhood of the shock waves, that is in a context which is quite far from the present work. Conversely, in [9,37] the second viscosity is used to speed up the convergence towards the asymptotic solution in the pseudo-time for incompressible NSEs (see also *e.g.* [24]). The above context is closer to the approach presented in this paper.

3. Brief recall of the δ^+-SPH scheme

In the present section we briefly introduce the δ^+-SPH scheme defined in [64] and further inspected in [5] which is the reference model for the simulations shown in the sequel. Applications to different weakly-compressible SPH schemes are provided in the Section §5.

The governing equations (1) are discretized as a set of fluid particles whose masses m_i maintain constant during the motion. The particles are initially placed on a lattice with homogeneous spacing Δr, and the initial particles' volumes V_i are set equal to Δr^n where n is the number of spatial dimensions. The particle masses m_i are calculated through the relation $m_i = \rho_i V_i$, using the initial density field. The same expression is used during the evolution to update the volumes from the solution of the density field.

For the sake of brevity, throughout the paper the notation $\boldsymbol{r}_{ji}$ indicates the differences of the particles positions, that is $\boldsymbol{r}_{ji} = \boldsymbol{r}_j - \boldsymbol{r}_i$. The same notation is used for the velocity fields $\boldsymbol{u}_{ji}$ and $\delta\boldsymbol{u}_{ji}$, while, for the generic scalar field the notation f_{ij} just indicates the dependency of the field f on the indices i and j.

The spatial gradients are approximated through convolution summations with a kernel function W_{ij}. This function has a compact support whose reference length is denoted by h and referred to as smoothing length. As in [4] a C2-Wendland kernel [74] is adopted in the present work. For this kernel the radius of the support is $2h$. In the numerical simulations that follow the number of neighbouring particles is chosen as $2h = 4\Delta r$ in two dimensions and $2h = 3\Delta r$ in three dimensions. The spatial derivatives of the kernel function are represented as follows:

$$\nabla_i W_{ij} = \boldsymbol{r}_{ji} F_{ij}\,, \tag{5}$$

where the scalar function F_{ij} only depends on the particle distance $r_{ji} = \|\boldsymbol{r}_{ji}\|$ and it is strictly positive (see *e.g.* [14]).

The δ^+-SPH scheme, then, reads:

$$\begin{cases} \dfrac{\mathrm{d}\rho_i}{\mathrm{d}t} &= -\rho_i \displaystyle\sum_j (\boldsymbol{u}_{ji} + \delta\boldsymbol{u}_{ji}) \cdot \nabla_i W_{ij}\, V_j + \sum_j (\rho_j\, \delta\boldsymbol{u}_j + \rho_i\, \delta\boldsymbol{u}_i) \cdot \nabla_i W_{ij}\, V_j + \mathcal{D}_i^{\rho}\,, \\ \rho_i \dfrac{\mathrm{d}\boldsymbol{u}_i}{\mathrm{d}t} &= \boldsymbol{F}_i^p + \boldsymbol{F}_i^v + \boldsymbol{F}_i^{ad} + \rho_i \boldsymbol{g} + \displaystyle\sum_j (\rho_j\, \boldsymbol{u}_j \otimes \delta\boldsymbol{u}_j + \rho_i\, \boldsymbol{u}_i \otimes \delta\boldsymbol{u}_i) \cdot \nabla_i W_{ij}\, V_j\,, \\ \dfrac{\mathrm{d}\boldsymbol{r}_i}{\mathrm{d}t} &= \boldsymbol{u}_i + \delta\boldsymbol{u}_i, \quad V_i = m_i \,/\, \rho_i, \quad p = c_0^2(\rho - \rho_0), \end{cases} \tag{6}$$

where the indexes i and j refer to generic i-th and j-th particles. The term $\mathcal{D}_i^{\rho}$ is the numerical diffusive term introduced by [1] to filter out the spurious high-frequency noise in the pressure field, while the vector $\delta\boldsymbol{u}$ is the Particle Shifting velocity used to regularize the particles' spatial distribution during their motion. The specific shifting velocity adopted in the present work is described in [51]. Accordingly, the time derivative d/dt indicates a quasi-Lagrangian derivative, *i.e.*:

$$\frac{d(\bullet)}{dt} := \frac{\partial(\bullet)}{\partial t} + \nabla(\bullet) \cdot (\boldsymbol{u} + \delta\boldsymbol{u})\,,$$

since the particles are moving with the modified velocity $(\boldsymbol{u} + \delta\boldsymbol{u})$ and the above equations are written in an Arbitrary-Lagrangian-Eulerian framework (for details see [5]). In the present scheme the Particle Shifting velocity is updated in an explicit way during the time integration of the Eq. (6). Incidentally, we highlight that implicit Particle Shifting algorithms were recently developed (see *e.g.* [58]). It is worth noting that the shifting velocity close to the free surface has to be modified to be consistent with the kinematic boundary condition along such an interface. In particular, the normal component of $\delta\boldsymbol{u}$ to this interface has to be nullified while the tangential component is maintained unaltered (for more details see *e.g.* [64,31]).

Finally, the terms $\boldsymbol{F}_i^p$ and $(\boldsymbol{F}_i^v + \boldsymbol{F}_i^{ad})$ are the pressure and viscous forces acting on the particle i. The modelling of the latter is given in the subsection 3.1. Regarding the pressure force $\boldsymbol{F}^p$, following [63] this is expressed as:

$$\begin{cases} \boldsymbol{F}_i^p = -\sum_j \left(p_j + p_i\right) \nabla_i W_{ij} V_j + S_i \sum_j \nabla_i W_{ij} V_j \,, \\ S_i = \begin{cases} 2p_i & \text{for } p_i < 0 \text{ and } i \notin \mathscr{S}_F \,, \\ 0 & \text{elsewhere} \,, \end{cases} \end{cases} \tag{7}$$

where $\mathscr{S}_F$ denotes the region of the fluid domain close to the free surface, that is the free-surface particles and their neighbouring particles. The free-surface particles are detected through the algorithm described in [47]. The last term on the right side of the Eq. (7) leads to a switch in $\boldsymbol{F}_i^p$ from the "plus" formulation of the pressure gradient (namely, $p_j + p_i$) to the minus formulation (that is, $p_j - p_i$) in the fluid regions where the pressure p_i is negative. This switch allows removing the so-called "tensile instability" which is a numerical instability of the SPH scheme (see [70,52,17]).

The solid boundaries are discretized with fixed ghost particles which interact with the fluid particles to provide free-slip or no-slip boundary conditions (for more details see, for example, [15,42,43]).

3.1. Viscous forces

A way to discretize the first viscous component $\boldsymbol{F}^v$ of the momentum equation has been proposed in [54]:

$$\begin{cases} \boldsymbol{F}_i^v = \mu\, K \sum_j \pi_{ij} \nabla_i W_{ij} V_j \,, & \pi_{ij} := \dfrac{\boldsymbol{u}_{ji} \cdot \boldsymbol{r}_{ji}}{||\boldsymbol{r}_{ji}||^2} \,, \\ \mu\, K = \alpha\, \rho_0\, c_0\, h \,, & K = [2(n+2)] \,, \end{cases} \tag{8}$$

where α is a dimensionless constant which determines the intensity of the viscous force, while n is the number of spatial dimensions (see *e.g.* [53]). In the limit of the particle size Δr going to zero, the above equation approximates the following convolution integral:

$$\langle \boldsymbol{F}^v \rangle(\boldsymbol{r}) = \mu\, K \int_\Omega \frac{[\boldsymbol{u}(\boldsymbol{r}') - \boldsymbol{u}(\boldsymbol{r})]}{|\boldsymbol{r}' - \boldsymbol{r}|^2} \nabla W(\boldsymbol{r}' - \boldsymbol{r})\, d\boldsymbol{r}' \,. \tag{9}$$

In [20] it was demonstrated that the following limits hold true:

$$\lim_{h \to 0} \langle \boldsymbol{F}^v \rangle(\boldsymbol{r}) = \mu \left[\nabla^2 \boldsymbol{u}(\boldsymbol{r}) + 2\nabla(\nabla \cdot \boldsymbol{u}(\boldsymbol{r})) \right] , \tag{10}$$

where h is the smoothing length of the kernel W.

Regarding the second viscosity component $\boldsymbol{F}^{ad} = \lambda \nabla(\nabla \cdot \boldsymbol{u})$, a discretization within the SPH framework is given in [7] where an appropriate dissipation function depending on the rate of change of particle volume is introduced:

$$\begin{cases} \boldsymbol{F}_i^{ad} = \lambda \langle \nabla D_i \rangle = \lambda \sum_j \left(D_j + D_i \right) \nabla_i W_{ij} V_j \,, \\ D_k = \langle \nabla \cdot \boldsymbol{u} \rangle_k = \sum_l \boldsymbol{u}_{lk} \cdot \nabla_k W_{kl} V_l \,. \end{cases} \tag{11}$$

Hence the term D_k represents the divergence of the velocity field evaluated at the position of the generic k-th particle. For Δr going to zero, $\langle \boldsymbol{F}^{ad} \rangle$ becomes:

$$\langle \boldsymbol{F}^{ad} \rangle(\boldsymbol{r}) = \lambda \int_\Omega \int_\Omega (\boldsymbol{u}^\star - \boldsymbol{u}) \nabla W(\boldsymbol{r}^\star - \boldsymbol{r}') \nabla W((\boldsymbol{r}^\star - \boldsymbol{r}')\, d\boldsymbol{r}^\star\, d\boldsymbol{r}' \tag{12}$$

and, when the smoothing length goes to zero, the following limit holds true (see [7] for details):

$$\lim_{h \to 0} \langle \boldsymbol{F}^{ad} \rangle(\boldsymbol{r}) = \lambda\, \nabla(\nabla \cdot \boldsymbol{u}(\boldsymbol{r})). \tag{13}$$

The limits (10) and (13) give the following overall viscous contribution:

$$\lim_{h \to 0} \langle \nabla \cdot \mathbb{V} \rangle = \mu\, \nabla^2 \boldsymbol{u}(\boldsymbol{r}) + (\mu + \lambda_{eff})\, \nabla(\nabla \cdot \boldsymbol{u}(\boldsymbol{r})) \,, \tag{14}$$

where $\lambda_{eff} = \mu + \lambda$ is the effective second viscous coefficient of the SPH scheme. The latter viscous component acts like an acoustic damper removing the acoustic waves generated by the weakly-compressible assumption through the divergence of the velocity field. Trivially, its contribution is null for the incompressible component of solution of the NSEs, since the velocity divergence is equal to zero by definition.

As remarked in [14], the term $\boldsymbol{F}^v$ includes the viscous contribution $\mu\nabla(\nabla\cdot\boldsymbol{u})$ and, therefore, partially acts as an acoustic damper. However, many hydrodynamics problems, as those including water impacts, are characterized by high Reynolds numbers and, consequently, μ is bounded to be as small as possible (see, for example, in [50]). In this perspective, the possibility of increasing the damping of the acoustic waves through the second viscous parameter is of fundamental importance.

In the numerical scheme the second viscous coefficient is modelled as $\lambda = \alpha_2\,\rho_0\,c_0\,h$, similar to the expression for μ in the Eq. (8). The intensity of $\boldsymbol{F}^{ad}$ can be, therefore, increased by raising the dimensionless coefficient α_2, as discussed in Section 3.2.

3.2. Time integration

The system (6) is integrated in time by using a fourth-order Runge-Kutta scheme with frozen diffusion as described in [2]. The use of a frozen-diffusion algorithm allows for a restrained computational cost and its coupling with the fourth-order Runge-Kutta scheme proves to be stable, robust and reliable. The same approach is also applied to the vector $\delta\boldsymbol{u}$ vector which is kept constant during the Runge-Kutta sub-steps. The evaluation of the acoustic damper term requires a double loop on the overall set of particles, since the velocity divergence needs to be evaluated before entering in the loop for the interactions of the momentum equations. The extra CPU-cost for the double loop is about 20%.

The time step for the integration, Δt, is obtained as the minimum over the following bounds:

$$\begin{cases} \Delta t_v = \dfrac{1}{\alpha}\left(\dfrac{h}{c_0}\right), \quad \Delta t_a = 0.25\,\min_i\sqrt{\dfrac{h}{\|\boldsymbol{a}_i\|}}, \quad \Delta t_\delta = \dfrac{0.44}{\delta}\left(\dfrac{h}{c_0}\right), \\ \Delta t_c = K_c\left(\dfrac{h}{c_0}\right), \quad \Delta t_{ad} = \dfrac{K_c}{\alpha_2}\left(\dfrac{h}{c_0}\right), \\ \Delta t = \min(\Delta t_v\,,\Delta t_a\,,\Delta t_\delta\,,\Delta t_c\,,\Delta t_{ad})\,, \end{cases} \tag{15}$$

where $\|\boldsymbol{a}_i\|$ is the particle acceleration and K_c is the Courant-Friedrichs-Lewy number. It is worth noting that the value of K_c depends on the adopted scheme and on the chosen kernel function (*i.e.* the C2-Wendland kernel).

Since we are interested in problems involving water impacts, the Reynolds number is generally high and, consequently, α is rather small, ranging from 0 to 0.01. This implies that the constraint on Δt_v is the least restrictive. Similarly, the constraint on Δt_δ is always negligible since δ is fixed to 0.1 (see also [1]).

Conversely, the coefficient α_2 has to be large enough in order to damp out the acoustic waves generated during impact events and, at the same time, it has to be smaller than unity to avoid that Δt_{ad} becomes smaller than Δt_a and Δt_c. Generally, Δt_c represents the most restrictive condition and the choice of K_c is fundamental for the stability and accuracy of the adopted numerical model. For the δ^+-SPH, we found $K_c = 1.5$ to be a reliable choice, while $K_c = 1.3$ and $K_c = 1.0$ are chosen for the δ-SPH and for the Standard SPH model respectively when the acoustic damper is implemented (see Section §5).

In all the simulations that follow we set $\alpha_2 = 1$, since this allows for the largest dissipation of the acoustic waves without affecting the time step.

3.3. Energy conservation within the adopted SPH model

Following the analysis performed in [3] and in [50], we provide the energy balance for the particle system presented in the previous section. This can be briefly arranged as follows:

$$\dot{\mathcal{E}}_M + \dot{\mathcal{E}}_C - \mathcal{P}_{ext} = \mathcal{P}_V + \mathcal{P}_{ad} + \mathcal{P}_N\,, \tag{16}$$

where $\mathcal{E}_M$ is the mechanical energy of the particle system, composed of the kinetic energy $\mathcal{E}_K = \sum_i m_i\,||\boldsymbol{u}_i||^2/2$ and the potential energy $\mathcal{E}_P = \sum_i m_i\,g\,z_i$ (z_i being the vertical coordinate of the i-th particle), while $\mathcal{E}_C$ is the elastic potential energy:

$$\mathcal{E}_C = \mathcal{E}_C(\rho_0) + c_0^2\sum_j\left[\log\left(\frac{\rho_j}{\rho_0}\right) + \frac{\rho_0}{\rho_j} - 1\right]\rho_j\,V_j\,. \tag{17}$$

The external power $\mathcal{P}_{ext}$ is evaluated through the mutual interaction between fluid and solid particles, as detailed in [3] and [12]. The latter work also contains the expression for the power related to fluid-fluid particle interactions of the viscous forces, namely $\mathcal{P}_V$. Such a term is negatively-defined and, therefore, represents a dissipation (for more details see *e.g.* [14]).

The contribution related to the "acoustic damper" for fluid-fluid particle interactions is equal to:

$$\mathcal{P}_{ad} = \alpha_2\,\rho_0\,c_0\,h\sum_i\sum_j\left(D_j + D_i\right)\boldsymbol{u}_i\cdot\nabla_i W_{ij}V_iV_j$$

$$
\begin{aligned}
&= \alpha_2\,\rho_0\,c_0\,h\sum_i\sum_j \left(D_j + D_i\right)\left(\frac{\boldsymbol{u}_i-\boldsymbol{u}_j}{2}+\frac{\boldsymbol{u}_i+\boldsymbol{u}_j}{2}\right)\cdot\nabla_i W_{ij}V_iV_j\\
&= \alpha_2\,\rho_0\,c_0\,h\sum_i\sum_j \left(D_j + D_i\right)\frac{\boldsymbol{u}_i-\boldsymbol{u}_j}{2}\cdot\nabla_i W_{ij}V_iV_j\\
&= \alpha_2\,\rho_0\,c_0\,h\sum_i V_iD_i\sum_j \boldsymbol{u}_{ij}\cdot\nabla_i W_{ij}V_j = -\alpha_2\,\rho_0\,c_0\,h\sum_j D_j^2V_j\,,
\end{aligned}
\tag{18}
$$

where we used the decomposition $\boldsymbol{u}_i = (\boldsymbol{u}_i-\boldsymbol{u}_j)/2 + (\boldsymbol{u}_i+\boldsymbol{u}_j)/2$, the symmetry properties of the kernel gradient [see the equation (5)] and the definition of D_i. Similar to $\mathcal{P}_V$, $\mathcal{P}_{ad}$ is a purely dissipation term.

Finally, the power of the remaining terms of the scheme are in the $\mathcal{P}_N$ expression, decomposed as follows:

$$
\mathcal{P}_N := \mathcal{P}_\delta + \mathcal{P}_{\delta u} + \mathcal{P}_{tic}\,,
\tag{19}
$$

where $\mathcal{P}_\delta$ contains the effect of the density diffusion (see [3,50] for details on this term), and $\mathcal{P}_{\delta u}$ is the power associated with the particles shifting $\delta\boldsymbol{u}$. The expression of the latter contribution is given below:

$$
\begin{aligned}
\mathcal{P}_{\delta u} \;=\; & -\frac{1}{2}\sum_i\sum_j\left[(p_j+p_i)\,\delta\boldsymbol{u}_{ji} + \left(\frac{p_j}{\rho_j}-\frac{p_i}{\rho_i}\right)(\,\rho_j\,\delta\boldsymbol{u}_j + \rho_i\,\delta\boldsymbol{u}_i\,)\right]\cdot\nabla_i W_{ij}\,V_i\,V_j\\
& -\frac{1}{2}\sum_i\sum_j\left[\left(\rho_j\,\boldsymbol{u}_j\otimes\delta\boldsymbol{u}_j + \rho_i\,\boldsymbol{u}_i\otimes\delta\boldsymbol{u}_i\right)\nabla_i W_{ij}\right]\cdot\boldsymbol{u}_{ji}\,V_i\,V_j\,.
\end{aligned}
\tag{20}
$$

The last term in $\mathcal{P}_N$ takes into account the energy contribution given by the pressure switch in Eq. (7):

$$
\mathcal{P}_{tic} = -\sum_i\sum_j (S_j\,\boldsymbol{u}_j - S_i\,\boldsymbol{u}_i)\cdot\nabla_i\,W_{ij}\,V_i\,V_j\,.
\tag{21}
$$

The energy related to this term is the one spent to prevent the tensile instability in negative pressure regions. It is worth noting that $\mathcal{P}_N$ is not a strictly dissipation term, although it includes the energy contributions from the pressure switch and the PST which guarantee the stability of the numerical scheme even when α and α_2 are zero. In particular, $\mathcal{P}_{\delta u}$ and $\mathcal{P}_{tic}$ can be largely positive, this meaning that the PST and the pressure switch can introduce energy in the system to maintain the particles spatial distribution ordered. Conversely, $\mathcal{P}_\delta$ is essentially a dissipation term (see, for example, [3]) and it is generally dominant with respect to $(\mathcal{P}_{\delta u}+\mathcal{P}_{tic})$. The energy dissipated by the scheme, $\mathcal{E}_{diss}$, is expressed as:

$$
\begin{cases}
\mathcal{E}_{diss} = \mathcal{E}_V + \mathcal{E}_{ad} + \mathcal{E}_N\,,\\[2ex]
\mathcal{E}_V := \displaystyle\int_{t_0}^{t}\mathcal{P}_V\,dt\,, \quad \mathcal{E}_{ad} := \int_{t_0}^{t}\mathcal{P}_{ad}\,dt\,, \quad \mathcal{E}_N := \int_{t_0}^{t}\mathcal{P}_N\,dt\,.
\end{cases}
\tag{22}
$$

As discussed in [45], during liquid impacts a sudden energy loss occurs. The weak-compressibility assumption, underlying the present scheme, implies that during these events a portion of the mechanical energy is converted into internal compressible energy in the form of acoustic waves. This part is mainly dissipated by $\mathcal{E}_N$ and by the "acoustic damper" term. The remaining portion is absorbed by the energy component $\mathcal{E}_V$, as shown in [50]. This latter term becomes more important with respect to the numerical dissipation when impacts are absent.

4. Test cases: application of the acoustic damper term to the δ^+-SPH model

In the present section we consider four benchmarks in order to show the benefits of the proposed acoustic damper term on different problems.

- The first benchmark describes the impacts of inviscid fluid patches in absence of solid boundaries. These problems are characterized by an intense generation of acoustic waves and, thus, are used to prove the effectiveness of the proposed acoustic damper term.
- The second and the third test cases are dedicated to the evolution of dam break flows and to their violent interaction with solid walls. In particular the second test-case concerns a classical benchmark widely used in the SPH community, while the third benchmark considers a three-dimensional dam break flow against a square cuboid.
- The fourth benchmark concerns a viscous flow past an elliptic cylinder. This case shows that the presence of the viscous term $\boldsymbol{F}^{ad}$ does not alter the drag and lift forces when the periodic regime is reached.

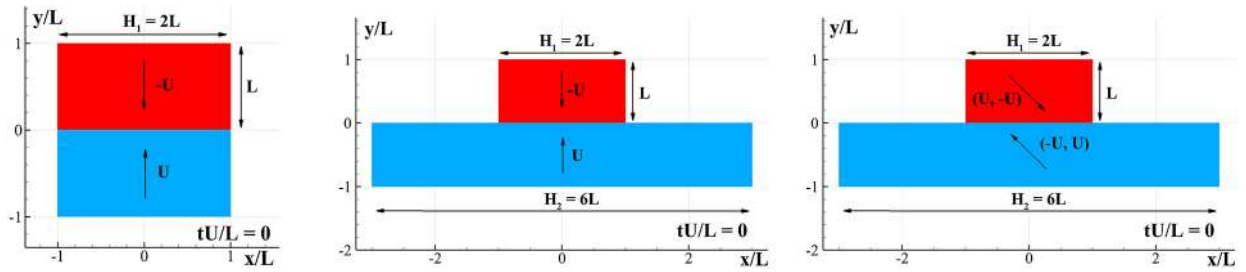

Fig. 2. Sketches of the impact of two water jets. Left: normal impact of 2D water-jets with the same masses; middle: normal impact of 2D water-jets with different masses; right: oblique impact of 2D water-jets with different masses.

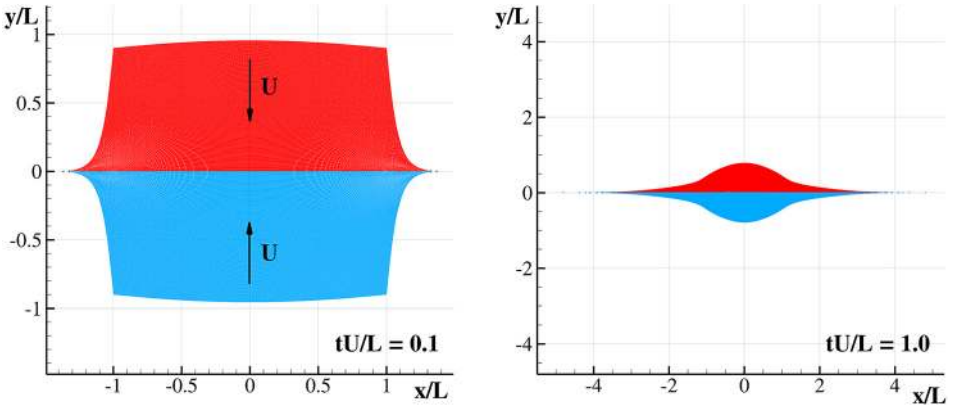

Fig. 3. Normal impact of 2D water-jets with the same masses ($L/\Delta r = 200$). Particles initially belonging to different fluid patches are plotted with different colours.

4.1. Impact of two water jets in 2D

Following [45], in the present section the impact of two rectangular patches of fluid is considered. Three different cases, respectively the normal impact of 2D water-jets with the same masses, the normal impact of 2D water-jets with different masses and the oblique impact of 2D water-jets with different masses, are simulated. The geometrical configurations of the problems are sketched in Fig. 2. The parameters used in the numerical simulations are $L = 1$ m, $U = 1$ m/s, $\rho = 1$ kg/m^3, $c_0 = 100$ m/s, $\alpha = 0.001$ and $\alpha_2 = 1$ or 0. The SPH results with and without the use of the acoustic damper term are compared and analyzed.

Following [53], at the highest resolution $L/\Delta r = 200$ and at $\alpha = 10^{-3}$, the equivalent Reynolds number, $\mathrm{Re} = UL/\nu$, is about 8,000 which is high enough to consider the liquid impact practically inviscid.

We first focus on the normal impact of two fluid patches with the same masses. The initial stages of the evolution are drawn in Fig. 3. During this phase, a large number of acoustic waves are generated as a consequence of the impact and spread all over the fluid domain. As shown in the upper panels of Fig. 4, the use of the acoustic damper term drastically reduces the occurrence of these waves in comparison to the version without it (bottom panels). Fig. 5 shows the evolution of the total mechanical energy $\mathcal{E}_M$ and compares it to the analytical solution derived for an inviscid incompressible fluid in [45]. The behaviour of the different energy contributions with (bottom) and without (top) the acoustic damper term unveils that in the former case the dissipation due to the acoustic damper term, namely $\mathcal{E}_{Ad}$, plays a major role in comparison to the term $\mathcal{E}_N$ that, on the contrary, is the principal source of dissipation in the scheme with $\alpha_2 = 0$. In particular Fig. 6 shows that the presence of the acoustic damper reduces the amount of energy that is dissipated by the viscous term, namely $\mathcal{E}_V$.

Comparing the top and middle plots of Fig. 7, for all the spatial resolutions the scheme with the acoustic damper term converges faster to the analytical solution with respect to the scheme without it. The convergence, however, becomes slower as the resolution increases (see the middle plot of Fig. 7). This behaviour is a consequence of the decrease in magnitude of the second viscous coefficient in the acoustic damper term, as $\lambda = \alpha_2 \rho_0 c_0 h = O(h)$ (see the equation (11)). Despite this, the acoustic damper term is still effective at fine resolutions, because of the larger generation of acoustic frequencies after the impact.

The bottom plot of Fig. 7 depicts the evolution of the total mechanical energy $\mathcal{E}_M$ for the spatial resolution $L/\Delta x = 100$ and $\alpha_2 = 1, 2, 4$. The results show that, for a given spatial resolution, the increase of α_2 corresponds to an increase of the damping of the acoustic waves. In any case, for $\alpha_2 \geq 1$ the stability constraint in Eq. (15) implies the decrease of the CFL factor K_c, leading to an increase of the CPU costs.

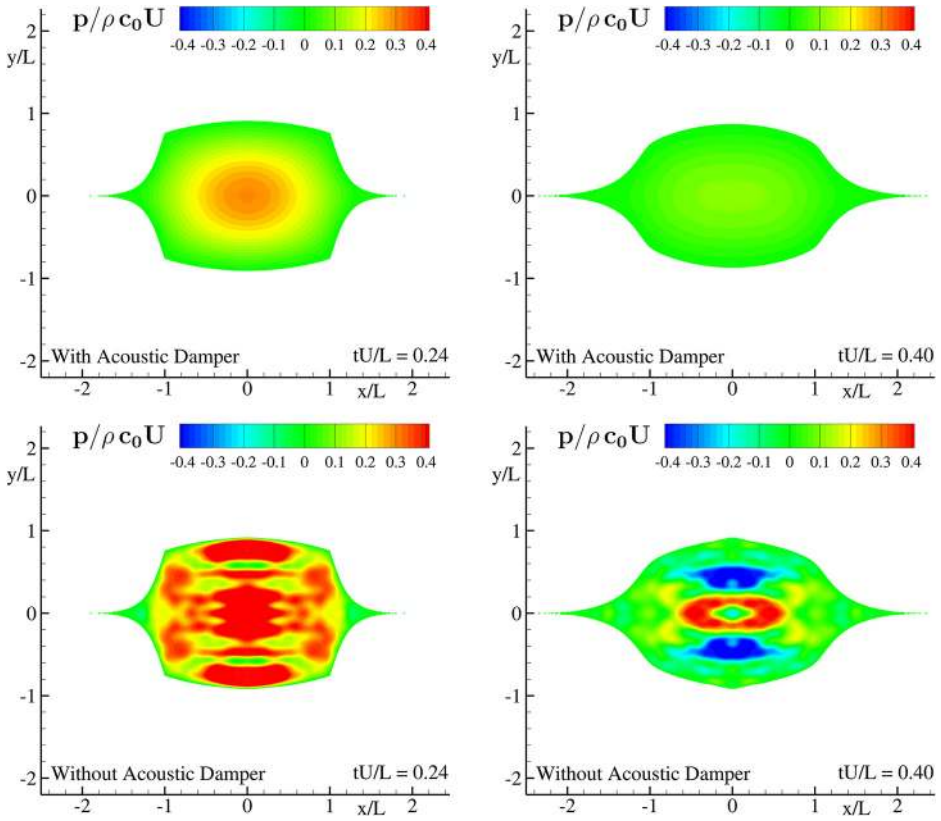

Fig. 4. Normal impact of 2D water-jets with the same masses ($L/\Delta r = 200$). Evolution of the pressure field with (top) and without (bottom) the acoustic damper term.

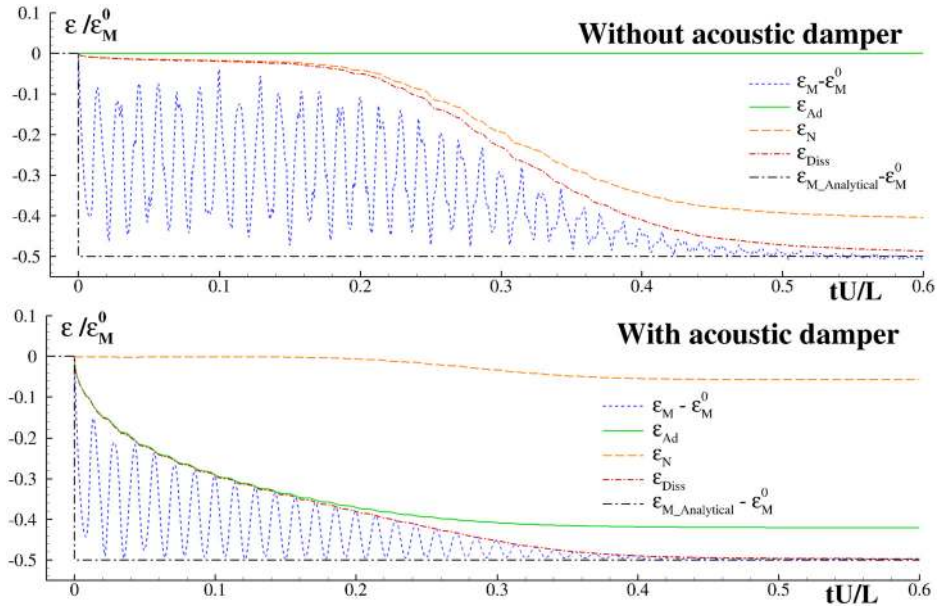

Fig. 5. Normal impact of 2D water-jets with the same masses ($L/\Delta r = 200$). Evolution of the total mechanics energy with (bottom) and without (top) the acoustic damper term. The symbol $\mathcal{E}_M^0$ denotes the global mechanical energy at the initial time.

As a second example, we deal with the normal impact of two fluid patches with different masses. Some snapshots of the initial configuration and of the subsequent evolution are sketched in Fig. 8 for $L/\Delta r = 200$. In this case two jets generate

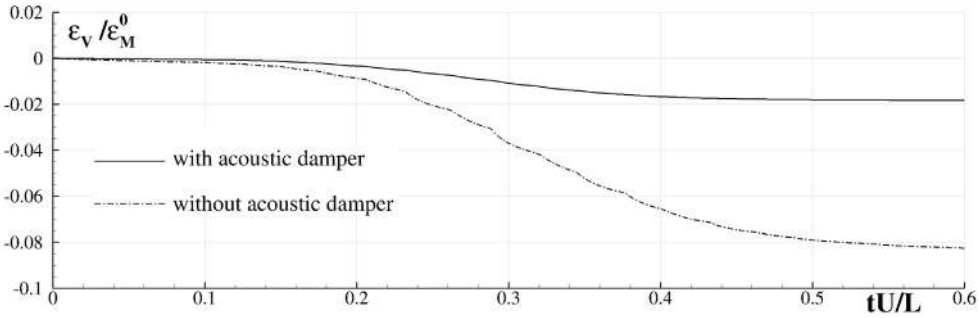

Fig. 6. Normal impact of 2D water-jets with the same masses ($L/\Delta r = 200$). Evolution of the energy related to the artificial viscous term with (solid line) and without (dashed-dotted line) the acoustic damper term.

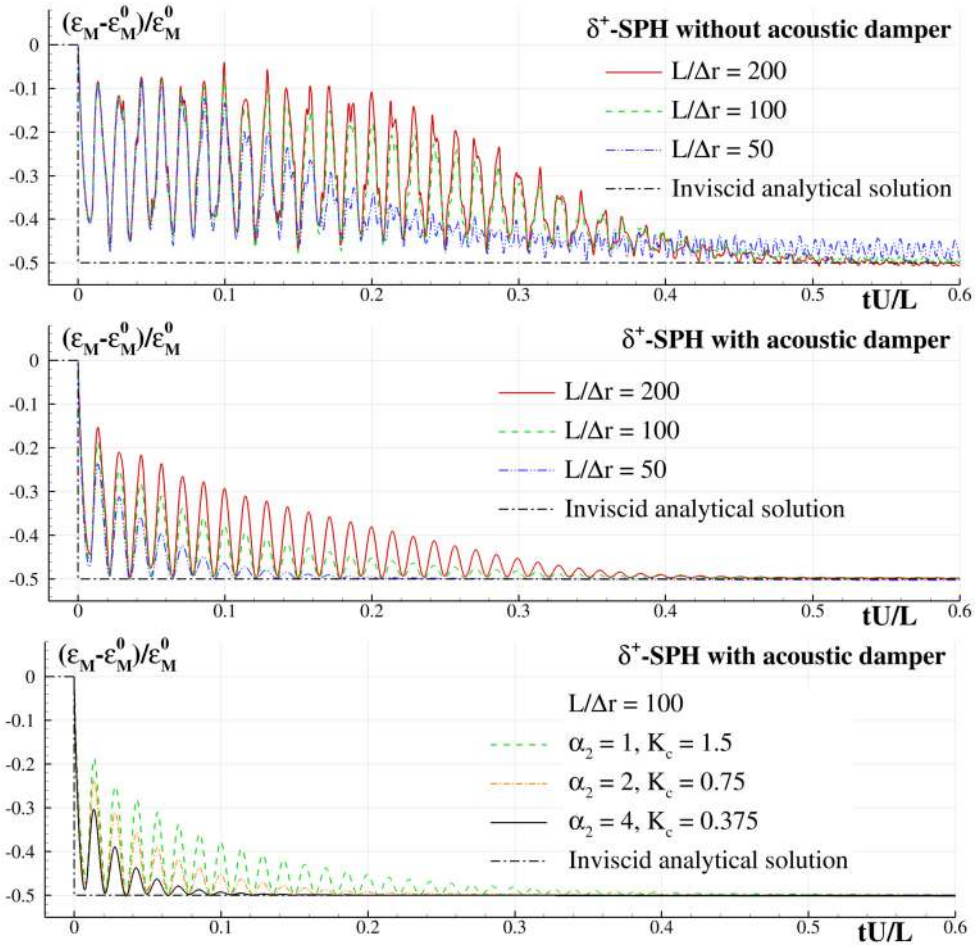

Fig. 7. Normal impact of 2D water-jets with the same masses. Evolution of the total mechanical energy without (top) and with (middle) the acoustic damper term (α_2 = 1) for different spatial resolutions. Evolution of the total mechanical energy with $L/\Delta r = 100$ and different values of α_2 (bottom). The symbol $\mathcal{E}_M^0$ denotes the global mechanical energy at the initial time.

at the extremities of the smaller patch and evolve as thin elongated filaments of fluid. The time history for three different spatial resolutions is displayed in Fig. 9 along with the theoretical solution for inviscid fluid (black solid line).

Finally, an oblique impact between patches with different masses is considered (see Fig. 10) for $L/\Delta r = 200$. In this case, in addition to the thin fluid filaments described previously, a sort of Kelvin-Helmholtz instability occurs between the two fluid patches, with a consequent generation of small vortical structures. Due to the presence of the artificial viscous force (see Eq. (8)), such small-scale vortexes induce an increase of the energy dissipation in comparison to the previous test cases. Despite this, the evolution of the mechanical energy (see Fig. 11) shows that the numerical scheme correctly converges towards the inviscid analytical solution, apart from a small deviation.

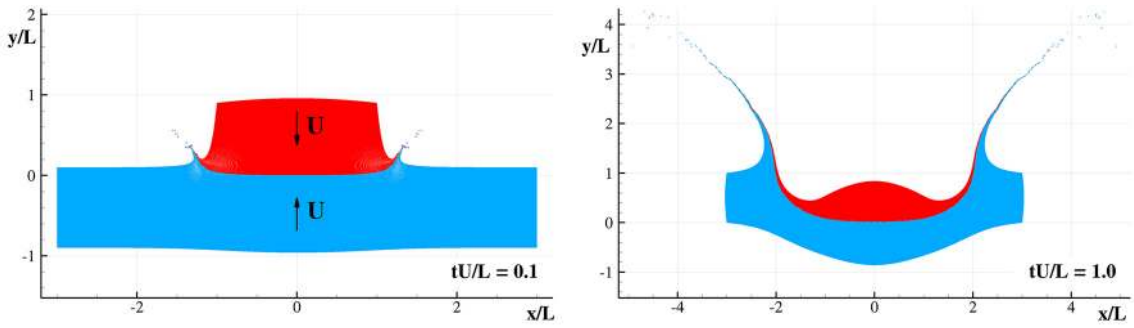

Fig. 8. Normal impact of 2D water-jets with different masses ($L/\Delta r = 200$). Particles initially belonging to different fluid patches are plotted with different colours.

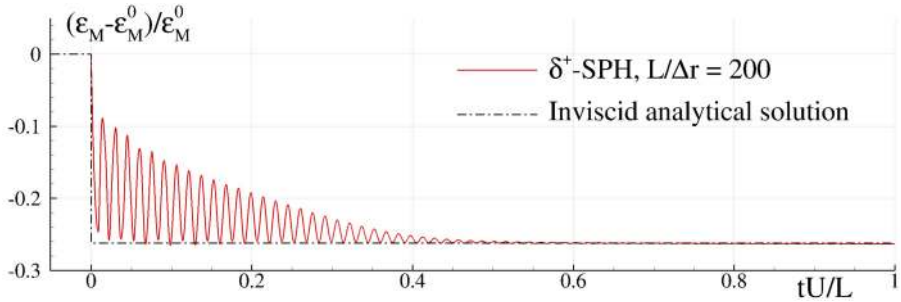

Fig. 9. Normal impact of 2D water-jets with different masses. Time evolution of the mechanical energy. The symbol $\mathcal{E}_M^0$ denotes the global mechanical energy at the initial time.

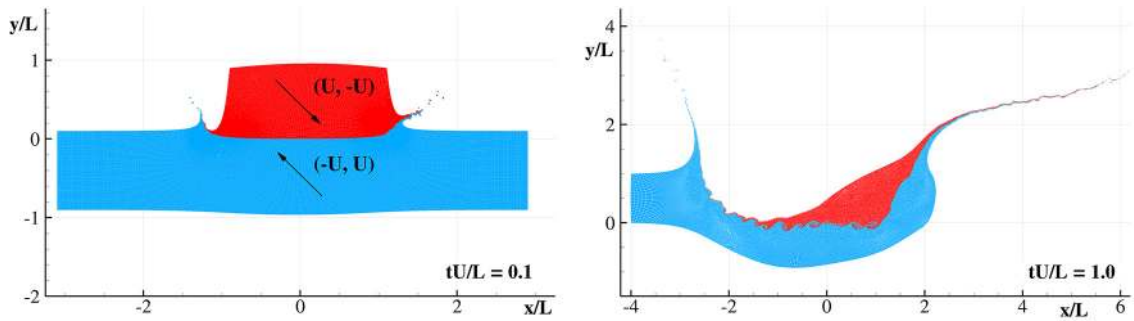

Fig. 10. Oblique impact of 2D water-jets with different masses ($L/\Delta r = 200$). Particles initially belonging to different fluid patches are plotted with different colours.

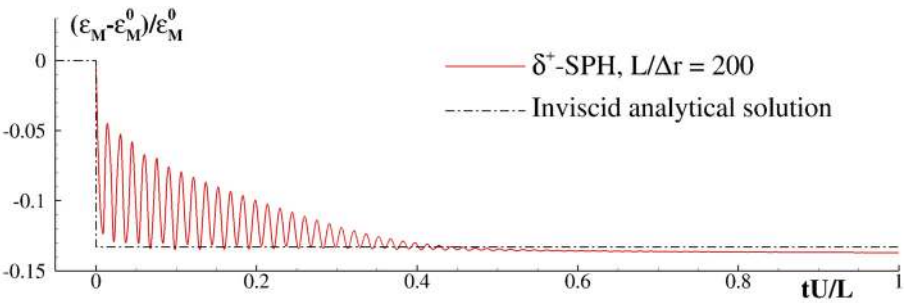

Fig. 11. Oblique impact of 2D water-jets with different masses. Time evolution of the mechanical energy. The symbol $\mathcal{E}_M^0$ denotes the global mechanical energy at the initial time.

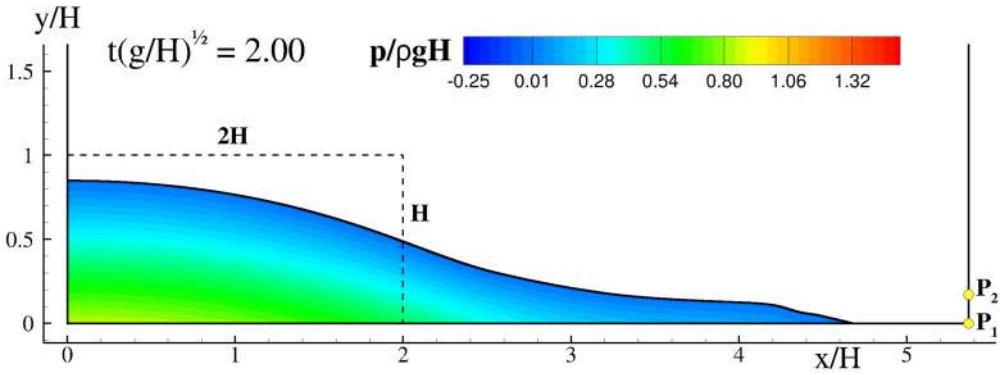

Fig. 12. Dam-break flow of a water column of height H and width $2H$ (resolution $H/\Delta r = 400$). The colours are representative of the pressure field.

4.2. Dam-break flow against a vertical wall

Here the effectiveness of the acoustic damper force is tested by simulating a dam-break flow impacting against a vertical wall. This is one of the most used benchmarks within the SPH community and for more information and details the interested reader is addressed to the works [42,39,46].

Fig. 12 shows the dam-break flow generated by the gravity collapse of a water column of height H and width $2H$. The fluid is confined in a rectangular tank of length $L = 5.366H$ and height $5H$. After the break of the dam, it evolves rightwards, impacts against the tank wall and generates a reverse flow with a plunging breaking wave. During the evolution, the pressure at the probes P_1 $(y = 0.01H)$ and P_2 $(y = 0.17H)$ along the right wall is recorded. Different from [42], the signals at the probes have not been filtered in time nor spatially averaged on the probe areas.

Ten different simulations were performed with five different spatial resolutions, namely $H/\Delta r = 50, 100, 200, 400, 800$, with and without the acoustic damper term (*i.e.* $\alpha_2 = 1$ and $\alpha_2 = 0$).

As described in [42], the maximum pressure peak predicted at the first impact by the potential flow theory is of order $p_{max} \approx 3\,\rho\,g\,H$. Consequently, the constraint of Eq. (2) implies that the speed of sound should satisfy $c_0 > 17.3\sqrt{gH}$. For this reason, the speed of sound is set equal to $c_0 = 20\sqrt{gH}$ and the artificial viscosity is $\alpha = 0.005$ in order to minimize the numerical dissipation. Following [53], the equivalent Reynolds number, $\mathrm{Re} = \sqrt{gH}H/\nu$, for the highest resolution (namely $L/\Delta r$ = 800) is about 32,000.

Figs. 13 and 14 display some snapshots of the evolution of the pressure field with and without the use of the acoustic damper term. Remarkably, this term is able to remove the largest part of the acoustic noise not only during the initial fluid impact against the solid wall (panels *a* and *b*), but also during the later evolution characterized by the closure of the plunging wave cavity (panel *c*) and by the subsequent splash-up cycles (panels *d* and *e*). The genesis of intense acoustic waves after the cavity closure is also commented in detail in [6].

Further, the noise-free pressure field displayed in Fig. 14 allows for a clear detection of the intense vortical structures generated by the splash-up events. The core of these eddies is characterized by an intense pressure drop (*i.e.* the dark blue spots in the panels at $t\sqrt{g/H} = 10.4$ and 20.0) which is completely hidden by acoustic waves when the acoustic damper term is not used. Fig. 15 depicts the contour of the vorticity field at times $t\sqrt{g/H} = 10.40$ and 20.00 when the above-mentioned eddies can be clearly identified.

In comparison with the solution presented in [5] the speed of sound is here doubled (namely $c_0/\sqrt{gH} = 20$ against 10) and the parameter α is halved. This implies that the generation of acoustic waves occurs earlier with respect to the results described in [5]).

The behaviour of the scheme at different spatial resolutions is described in Fig. 16 where the pressure signal at the probe P_1 is displayed with and without the acoustic damper term. As expected, the pressure oscillations increase as the spatial resolution increases, and this phenomenon also affects the scheme with the acoustic damper term, because its magnitude lessens as h decreases (see Eq. (11)). Notwithstanding this, at each resolution, the scheme with the acoustic damper term shows a drastic reduction of the pressure oscillations in comparison to the scheme without it. A further dampening of this noise is possible by increasing the value of α_2 at the price of a smaller time step (see Section §3.2).

Regarding the energy balance of the scheme, it is useful to introduce the discard of the potential energy $\Delta\mathcal{E}$ as the difference between the initial condition, when the liquid is at rest on the left of the dam, and the asymptotic final configuration, when the liquid is at rest in the whole tank:

$$\Delta\mathcal{E} := \mathcal{E}_{M0} - \mathcal{E}_{M\infty} = \rho\,g\,H^3\left[1 - \frac{2H}{L}\right]. \tag{23}$$

The left panel of Fig. 17 displays the behaviour of the energy dissipated by the acoustic damper term scaled by $\Delta\mathcal{E}$ for $H/\Delta r = 100, 200, 400$. Surprisingly, the amount of dissipated energy only shows minor changes. This is due to two opposite

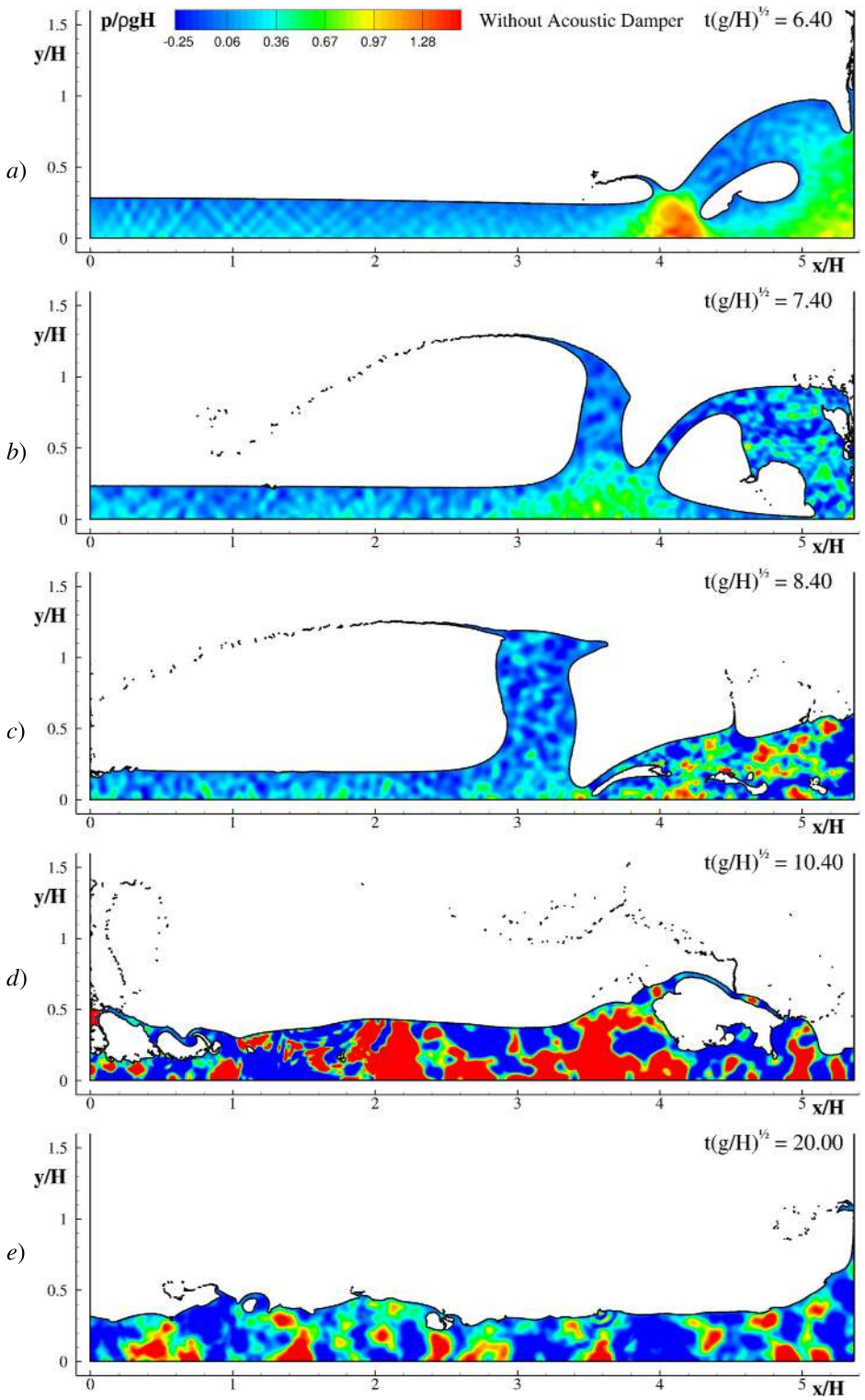

Fig. 13. Dam-break flow of a water column with $H/\Delta r = 400$, $\alpha = 0.005$, $\alpha_2 = 0.0$. The colours are representative of the pressure field.

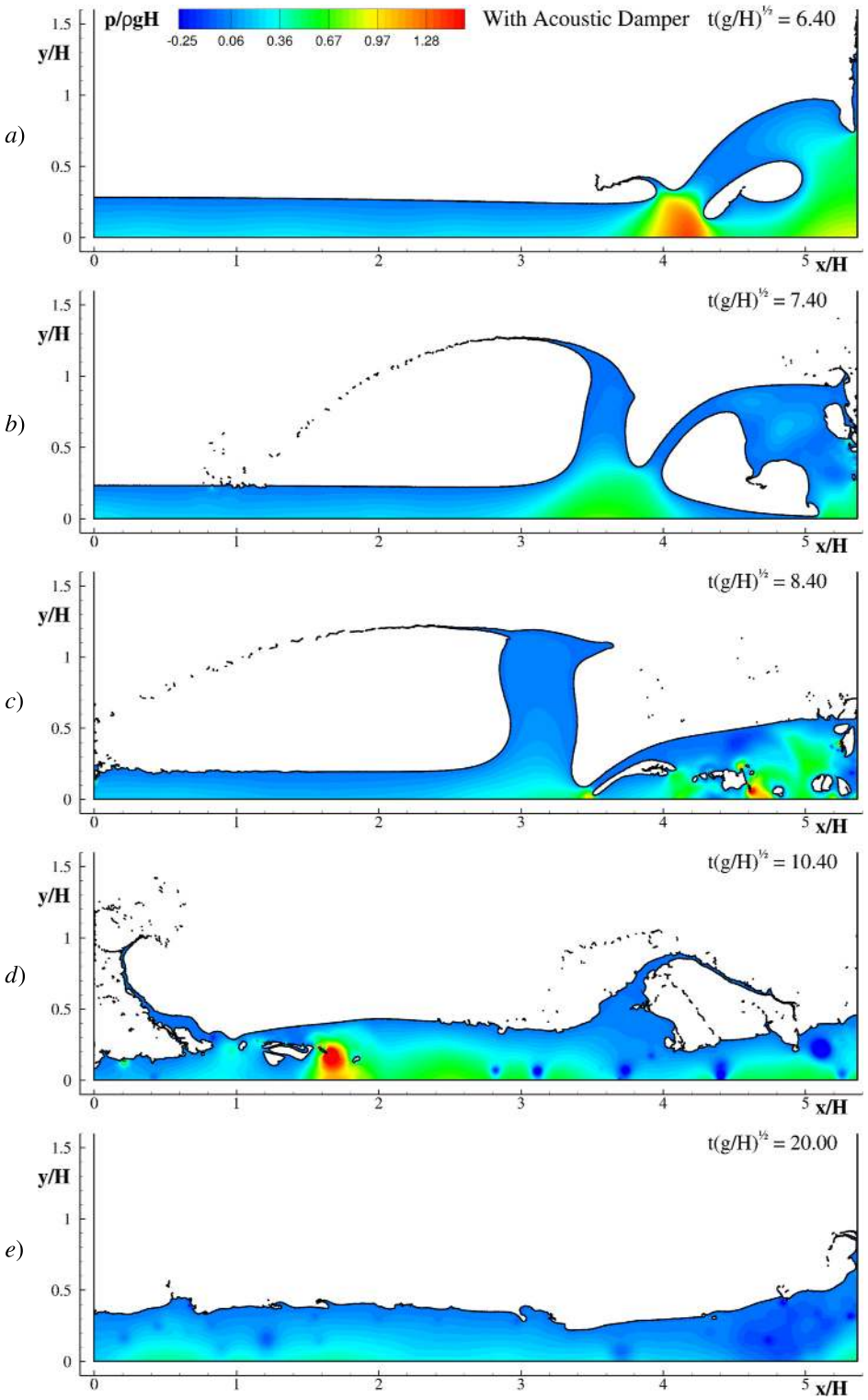

Fig. 14. Dam-break flow of a water column with $H/\Delta r = 400$, $\alpha = 0.005$, $\alpha_2 = 1.0$. The colours are representative of the pressure field.

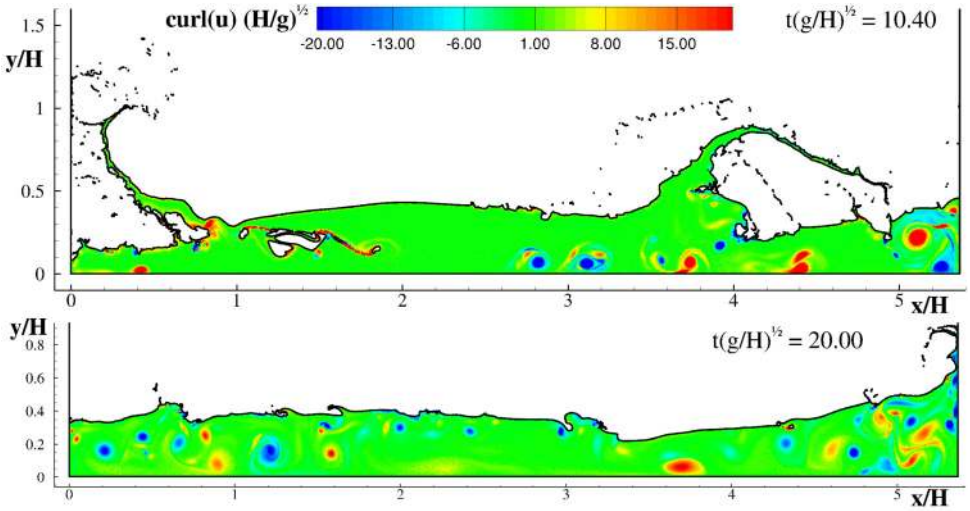

Fig. 15. Dam-break flow of a water column. $H/\Delta r = 400$, $\alpha = 0.005$, $\alpha_2 = 1.0$. Vorticity field during the splash-up stages at times $t\sqrt{g/H} = 10.4$ (top) and $t\sqrt{g/H} = 20.0$ (bottom).

phenomena that partially compensate as the spatial resolution increases: *i*) the reduction of the magnitude of the acoustic damper term as h goes to zero, *ii*) the increase of the acoustic noise.

Considering the evolution of the global mechanical energy of the particle system, the right panel of Fig. 17 shows that this is weakly influenced by the use of the acoustic damper term. This means that $\mathcal{E}_{diss}$ in Eq. (22) is approximately the same, implying that the energy dissipated by the acoustic damper, namely $\mathcal{E}_{ad}$, is replaced by the contributions $\mathcal{E}_V$ and $\mathcal{E}_N$ in the model without such a term. In any case, the action of the artificial viscosity and of the other numerical corrections is not enough to remove the acoustic waves generated during fluid-fluid and fluid-solid impacts.

Finally, Fig. 18 displays the comparisons between the numerical schemes with and without the acoustic damper term and the experimental measurements of [39] (top) and [10] (bottom). In all the cases the results obtained with the proposed term are in good agreement with the experiments and are free from the acoustic component. Incidentally, we observe that the deviation of the numerical signals from the experimental measurements for $t\sqrt{g/H} > 6$ is a consequence of the fact that the numerical simulations are single-phase and, therefore, cannot represent the phenomenon of air entrapment that occurs during the collapse of the plunging wave at the right wall (see, for example, [15]).

Before proceeding to the next section, we would like to discuss a further aspect. Following the approach described in [49], it is possible to filter the pressure field of the δ^+-SPH during the post-processing stage and recover a numerical solution that is close to that obtained through the acoustic damper term. The proposed scheme, however, allows for a direct evaluation of a smooth pressure field and, therefore, is expected to be suitable for problems where the fluid is coupled with an elastic structure (see *e.g.* [66,65,48]). In particular, the action of the acoustic damper term helps to remove the oscillations caused by the use of a numerical sound speed.

4.3. 3D dam-break flow against a square cuboid

To demonstrate the effectiveness of the acoustic damper term in preventing pressure noise in 3D problems, we consider a 3D dam break flow against a square box placed on the tank bottom. This benchmark was initially studied in [32] and has been extensively used to test different numerical schemes (see *e.g.* [36,44]).

Here, three different SPH models, respectively the δ^+-SPH, the δ-SPH and the Standard SPH schemes, are adopted with (*i.e.* $\alpha_2 = 1$) and without (*i.e.* $\alpha_2 = 0$) the proposed acoustic damper term. In all the SPH simulations, the same particle resolution (namely, $H/\Delta r = 55$) is adopted, which leads to about 1.3 million particles. The artificial sound speed is $c = 20\sqrt{gH}$ and $\delta = 0.1$ and $\alpha = 0.01$ are chosen for the density and viscosity diffusive terms.

Fig. 19 depicts the pressure distribution after the first fluid impact on the square cuboid obtained by the different SPH schemes. The effectiveness of the acoustic damper term in eliminating the acoustic waves originated at the liquid impact is evident. Comparing the sub-figures on the left and right columns for the δ^+-SPH and δ-SPH results (top and middle panels), it is possible to observe that the pressure field simulated with the acoustic damper term is free from any observable acoustic oscillation, while the results obtained without using this term show apparent large-scale pressure waves radiated from the impact position. Such kind of pressure waves are characterized by long wavelengths and cannot be prevented through the use of the traditional diffusive terms, since these mainly act on spurious oscillations with wavelengths comparable or smaller than the SPH kernel support.

The bottom panels of Fig. 19 further confirm the above behaviour when the acoustic damper term is implemented in the standard SPH scheme. In this latter case, however, some small-scale pressure noise still persists, proving that the density

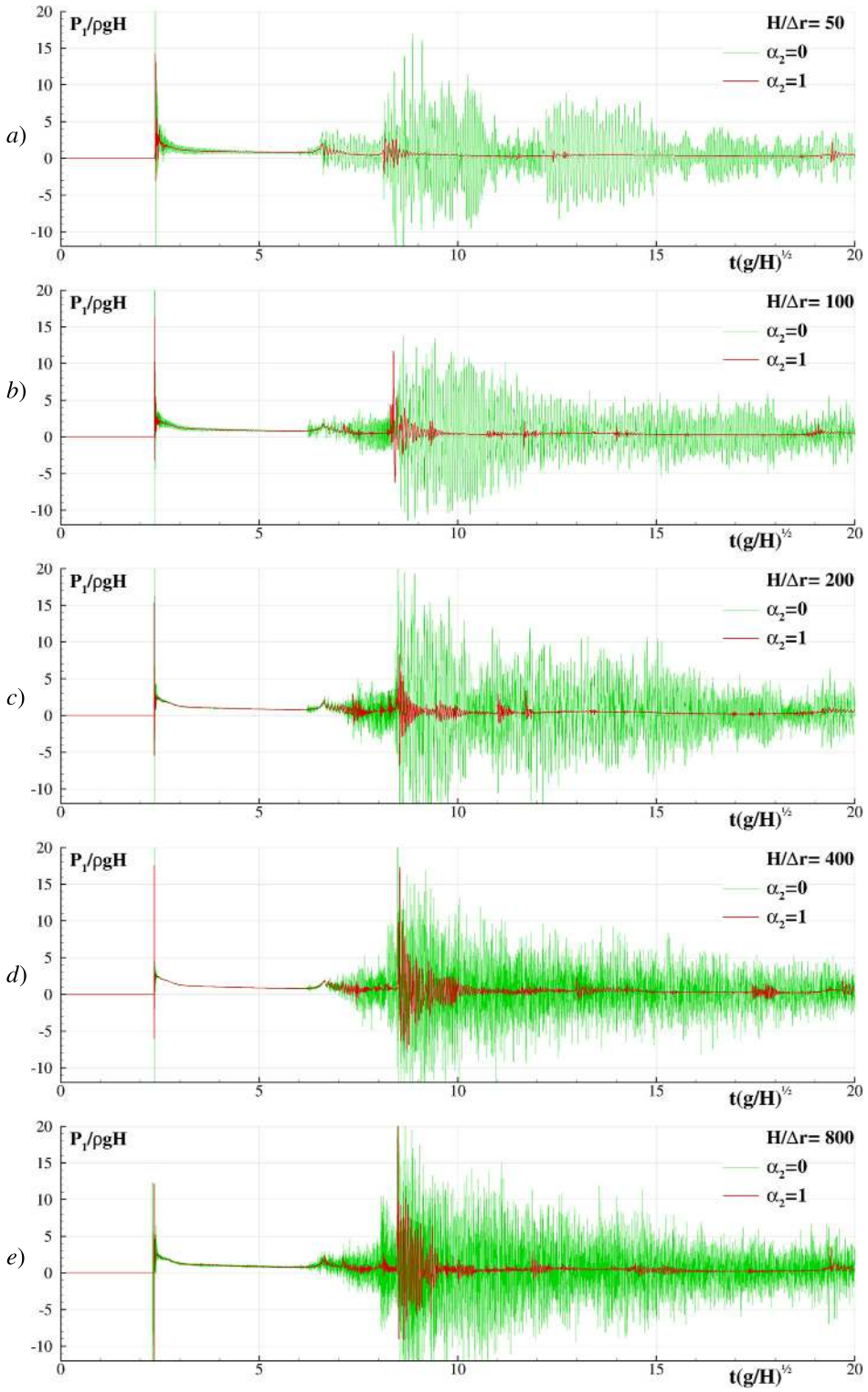

Fig. 16. Dam-break flow of a water column. Time histories of the pressure recorded at probe P_1 for different spatial resolutions. Cases with $\alpha_2 = 0$ and $\alpha_2 = 1$ refer to simulations without and with acoustic damper term respectively.

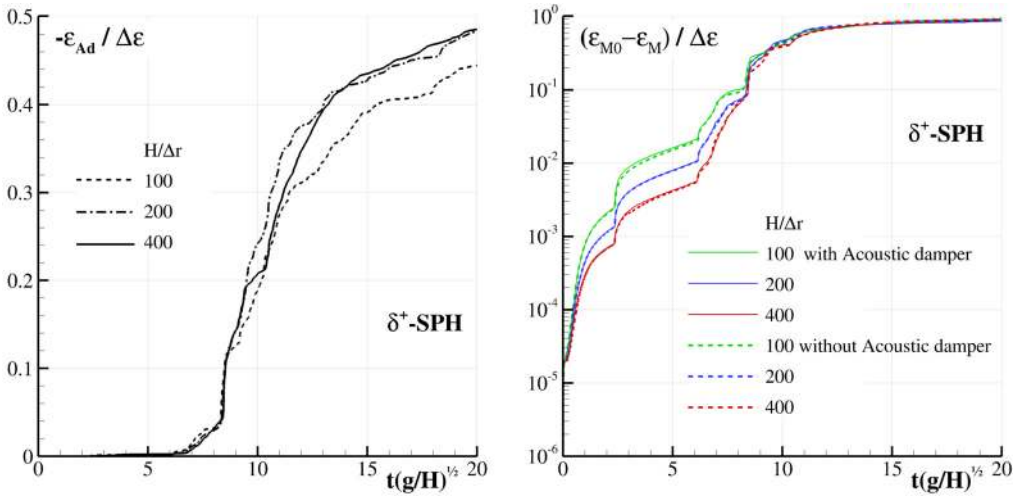

Fig. 17. Dam-break flow of a water column. Time histories of the energy dissipated by the acoustic damper term (left) and of the mechanical energy (right) for three different $H/\Delta r$ ratios.

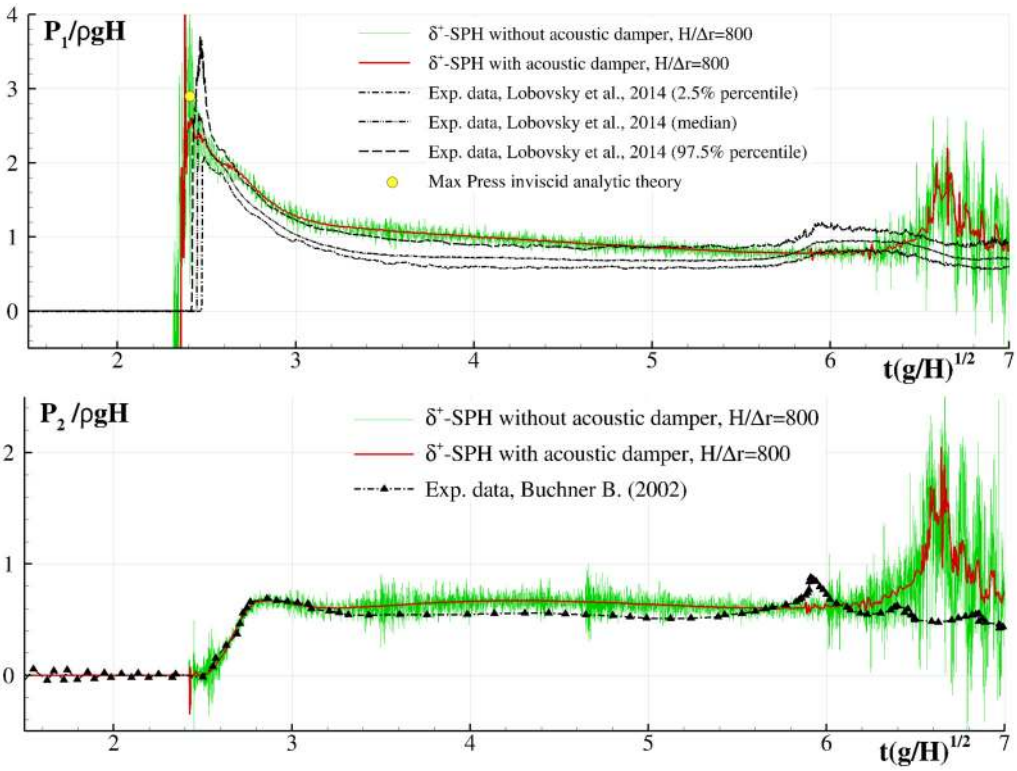

Fig. 18. Dam-break flow of a water column. Time histories of the pressure recorded at probe P_1 (top) and P_2 (bottom) using the highest spatial resolution $H/\Delta r = 800$. Comparisons against experimental data.

diffusive term is essential to get rid of this kind of spurious oscillations. The latter observation brings forward some of the conclusions attained from 2D studies in the Sections 5.1 and 5.2.

Finally, Figs. 20 and 21 show a lateral and a bottom view of the pressure fields at five different time instants as obtained through the δ^+-SPH with (left columns) and without (right columns) the acoustic damper term. From these plots it is evident that the acoustic waves generated by the liquid impact against the cuboid have a magnitude comparable with the hydrostatic pressure and that they can significantly change the local loads on the tank bottom and walls.

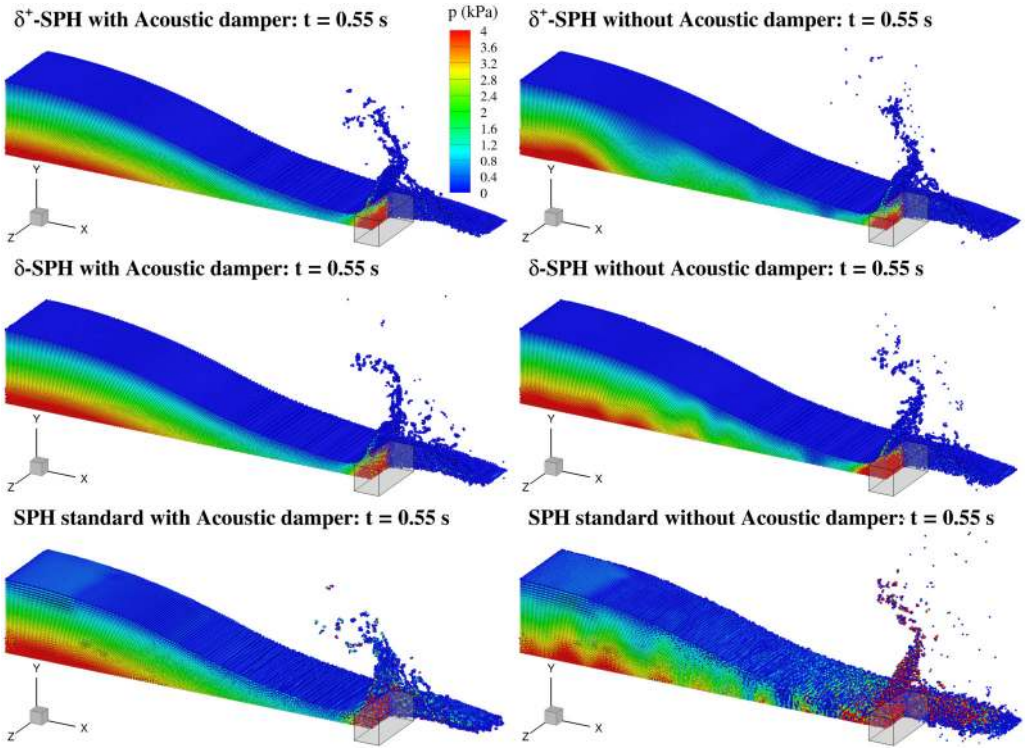

Fig. 19. 3D dam-break flow against a square cuboid: half flow domain is reported in order to show the pressure field at $t = 0.55$ s, obtained by using the δ^+-SPH (top), the δ-SPH (middle) and the Standard SPH (bottom) schemes with $H/\Delta r = 55$, $\delta = 0.1$, $\alpha = 0.01$, $\alpha_2 = 1$ (left) and $\alpha_2 = 0$ (right).

4.4. Inclined elliptic cylinder subjected to an unsteady current

In this subsection the viscous flow past an inclined elliptical cylinder is considered. The chord length of the profile is the major axis of the ellipse and it is indicated in the following text with the letter a. The ratio between the axes is equal to $b/a = 0.4$ and the angle of attack is 20°. The centre of the ellipse is placed at the origin of the frame of reference and the fluid domain is $[-4a, 11a] \times [-4a, 4a]$. An inflow boundary condition is enforced on the left side of the domain (*i.e.* $x = -4a$) while an outflow condition is implemented on the right side (namely, $x = 11a$). The inflow and outflow data are prescribed following the technique described in [21,43]. Finally, the horizontal planes $y = \pm 4a$ are modelled as impermeable boundaries where free-slip conditions are enforced.

A free stream with constant intensity U along the x-axis is considered in all the simulations and the speed of sound is set equal to $c_0 = 10U$. The Reynolds number, defined as $\mathrm{Re} = \rho U a/\mu$, is set equal to 1000. As described in [19], after a transitory stage the flow reaches a periodic regime with a typical von Kármán vortex shedding. In order to avoid an impulsive start, the final value of U is reached through an acceleration ramp described by:

$$U_\infty(t) = \begin{cases} \dfrac{U}{2}\left[1 - \cos\left(\dfrac{\pi t}{t_r}\right)\right], & t \le t_r, \\ U, & t > t_r, \end{cases} \quad \text{and} \quad A_\infty(t) = \begin{cases} \dfrac{U\pi}{2t_r}\sin\left(\dfrac{\pi t}{t_r}\right), & t \le t_r, \\ 0, & t > t_r, \end{cases} \tag{24}$$

where t_r is the time ramp and A_∞ is the free stream acceleration.

The plots in Fig. 22 show the pressure fields at time $tU/a = 0.4$ using two different time ramps, namely $t_r U/a = 1$ (top) and $t_r U/a = 1/4$ (bottom). Because of the initial acceleration, acoustic waves of different intensity are generated at the cylinder surface and radiated towards the domain boundaries. It is worth noting that the same problem was also studied in [64]. There, the longer time ramp, *i.e.* $t_r U/a = 1$, was adopted in order to reduce the generation of strong acoustic waves in the transitory stage. On the contrary, in the present work a shorter time ramp can be used thanks to the acoustic damper term, leading to a more rapid transitory stage.

The pressure field at the inflow/outflow boundaries is modified in order to let the acoustic waves cross them, as described in [34]. However, because of the lateral walls at $y = \pm 4a$, wave reflections remain within the fluid domain for a considerable time range. Fig. 23 shows the pressure fields at time $tU/a = 4.4$ evaluated by the δ^+-SPH method without (top) and with (bottom) the acoustic damper term. The presence of the acoustic waves is well visible in both the plots even if, when the acoustic damper is adopted, these waves are largely damped.

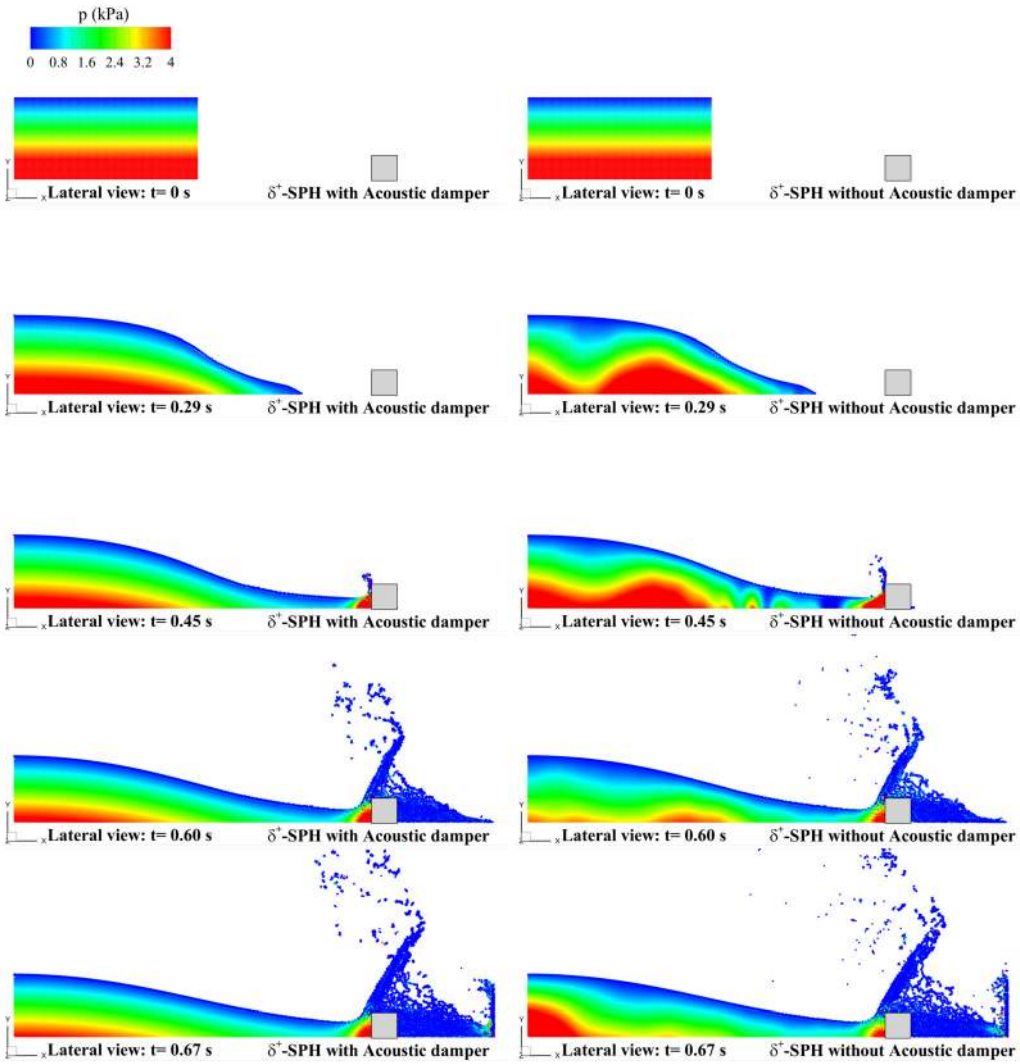

Fig. 20. 3D dam-break flow against a square cuboid: lateral view of the pressure field in the halved fluid domain for five different time instants, obtained by using the δ^+-SPH with $\alpha_2 = 1$ (left) and $\alpha_2 = 0$ (right).

The results obtained using the δ^+-SPH method are compared with the ones obtained through the Diffused Vortex Hydrodynamics (DVH). The latter is a Particle Vortex Method, extensively validated for the solution of planar viscous flows past rigid bodies (see *e.g.* [59,60]). We stress here that the DVH method solves the incompressible NSEs. Different from [64] where a wider channel was used ($10a$ against the $8a$ adopted here), the presence of the horizontal solid boundaries is also considered within the DVH. The comparisons are made in terms of drag c_D and lift c_L coefficients. The force coefficients are defined as:

$$c_D = \frac{F_x}{1/2\,\rho\,U^2\,a}\,, \qquad c_L = \frac{F_y}{1/2\,\rho\,U^2\,a}\,, \tag{25}$$

where ρ is the fluid density, F_x and F_y are the force components acting on the body along the x and y directions.

Fig. 24 depicts the time histories of c_D and c_L evaluated by the δ^+-SPH solver with and without acoustic damper. The SPH solutions are also compared against the DVH outputs. Without the acoustic damper term the forces are characterized by a high frequency noise which is caused by the acoustic wave reflections at the walls. On the contrary, these oscillations are lessened by the acoustic damper term and the agreement between the δ^+-SPH and the DVH drastically improves within the periodic regime (namely, for $tU/a > 25$).

This result clearly shows that the acoustic damper does not alter the divergence-free component of the velocity field and that it mainly acts to eliminate the component of acoustic waves. A further confirmation of the above statement is given in Fig. 25 where a comparison of the vorticity field at the instant when the maximum lift force occurs is sketched between the δ^+-SPH with the acoustic damper term and the DVH.

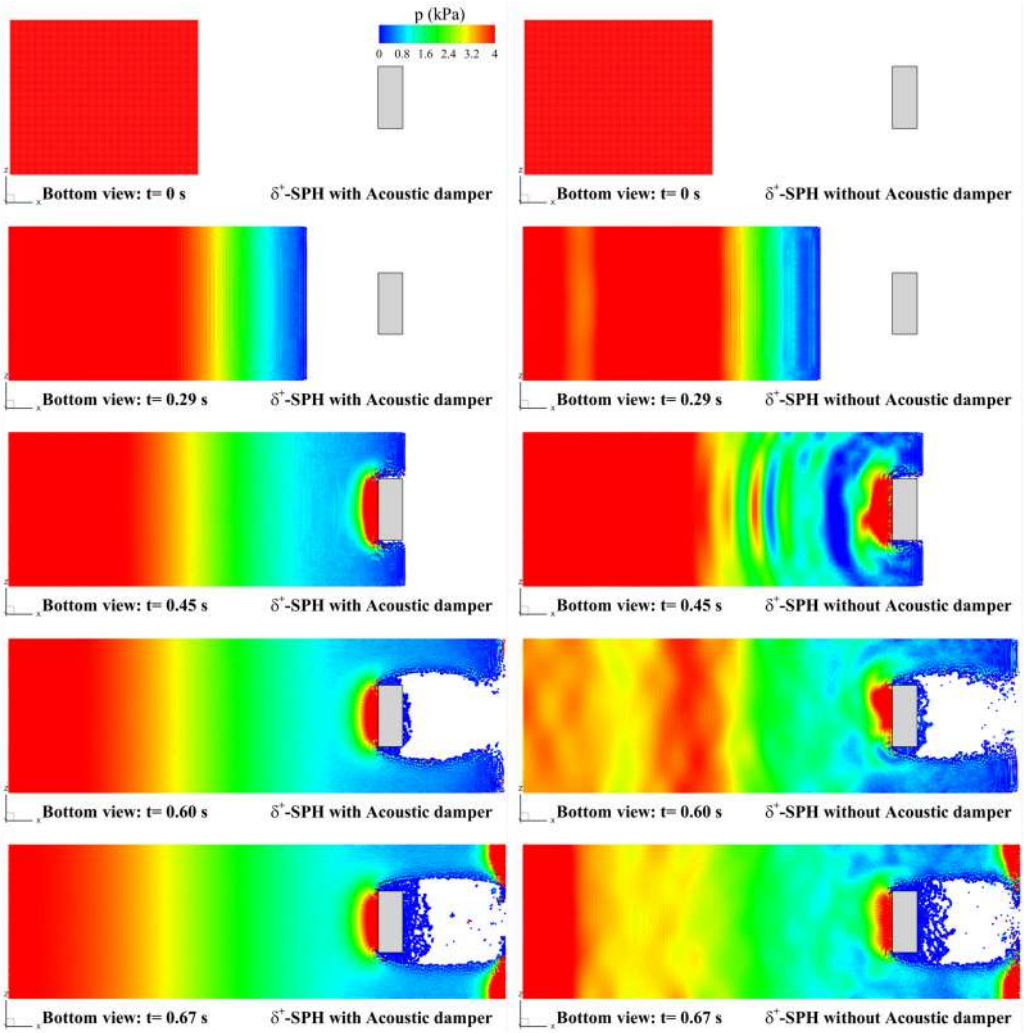

Fig. 21. 3D dam-break flow against a square cuboid: view of the pressure field from the bottom of the domain for five different time instants, obtained by using the δ^+-SPH with $\alpha_2 = 1$ (left) and $\alpha_2 = 0$ (right).

5. Application of the acoustic damper term to other weakly-compressible SPH models

In this section the acoustic damper term is implemented in three different weakly-compressible SPH models, namely the standard SPH model, the δ-SPH model and the δ^+-SPH model, to demonstrate its effectiveness, versatility and reliability. Two different cases are considered: the inviscid oscillating droplet described in subsection 5.1 and a shallow-water sloshing motion in subsection 5.2.

5.1. Inviscid oscillating droplet

The first test case is dedicated to the simulation of an inviscid droplet oscillating in an centripetal force field. This is a problem without solid boundaries nor water impacts and, for this reason, it is characterized by a small generation of acoustic waves. This benchmark, therefore, is used to check the accuracy and reliability of the acoustic damper term in problems where the viscous term $\boldsymbol{F}^{ad}$ is expected to play a minor role.

The droplet is initially circular with radius $R = 1$ and oscillates in a force field given by $-B^2\boldsymbol{r}$ where B is a dimensionless parameter. The velocity field in the droplet is

$$\boldsymbol{u}(x, y, t) = (A(t)x, -A(t)y), \tag{26}$$

and the analytical solution for $A(t)$ is described in [55]. Accordingly, the initial pressure in the droplet centre is given by:

$$p(x, y, t = 0) = \rho_0 \frac{(A^2 + B^2)}{2} \left(1 - x^2 - y^2\right). \tag{27}$$

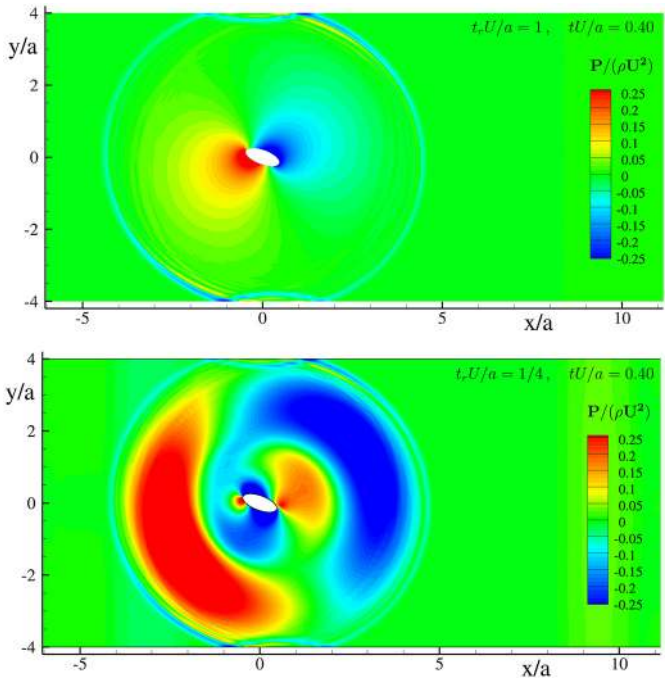

Fig. 22. Viscous flow past an inclined elliptic cylinder. Pressure field during the transitory stage at time $tU/a = 0.4$. Acoustic waves are generated by the acceleration of the inflow current starting from the rest condition. Top: using a time ramp $t_r U/a = 1$. Bottom: using a time ramp $t_r U/a = 1/4$.

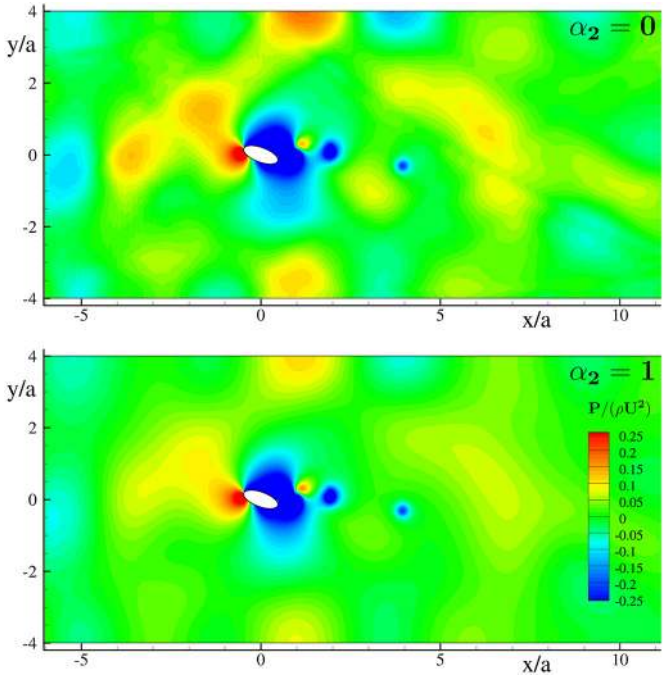

Fig. 23. Viscous flow past an inclined elliptic cylinder. Pressure field at time $tU/a = 4.4$ by using a time ramp $t_r U/a = 1/4$. Top: without acoustic damper. Bottom: with acoustic damper.

Here, we set $A(t = 0)/B = 1$ and consider $R/\Delta r = 100$ as reference particle resolution.

In previous studies, such a solution has been used for validating newly proposed SPH schemes. Similarly, in the present case inviscid SPH simulations are carried out by using the consistent δ^+-SPH model with the acoustic damper term. Specifically, we set $\alpha = 0$ and $\alpha_2 = 1$. Two snapshots of the evolution of the droplet and of the pressure field are displayed in Fig. 26.

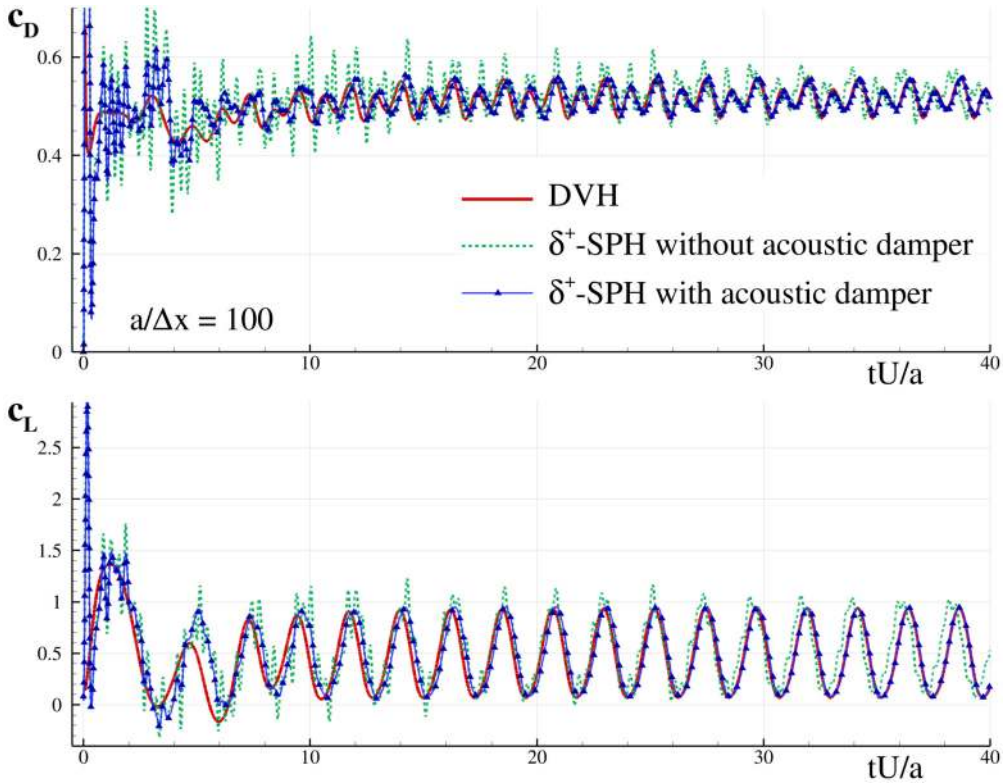

Fig. 24. Viscous flow past an inclined elliptic cylinder. Time histories of the drag (top) and lift (bottom) coefficients. The δ^+-SPH solutions with and without the acoustic damper term are compared against the DVH reference solution.

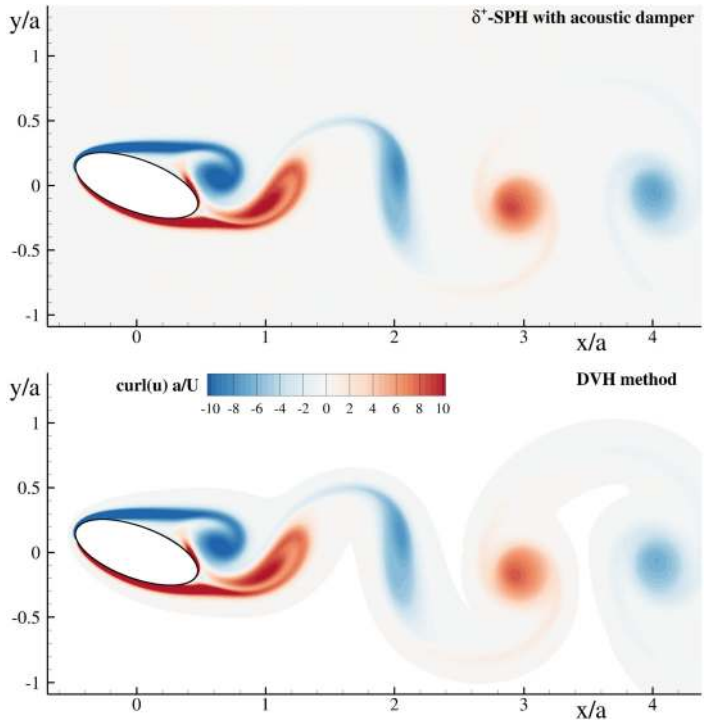

Fig. 25. Viscous flow past an inclined elliptic cylinder. Vorticity field in the near field evaluated at maximum lift force ($tU/a = 38.63$). Top: δ^+-SPH solutions with acoustic damper. Bottom: DVH method.

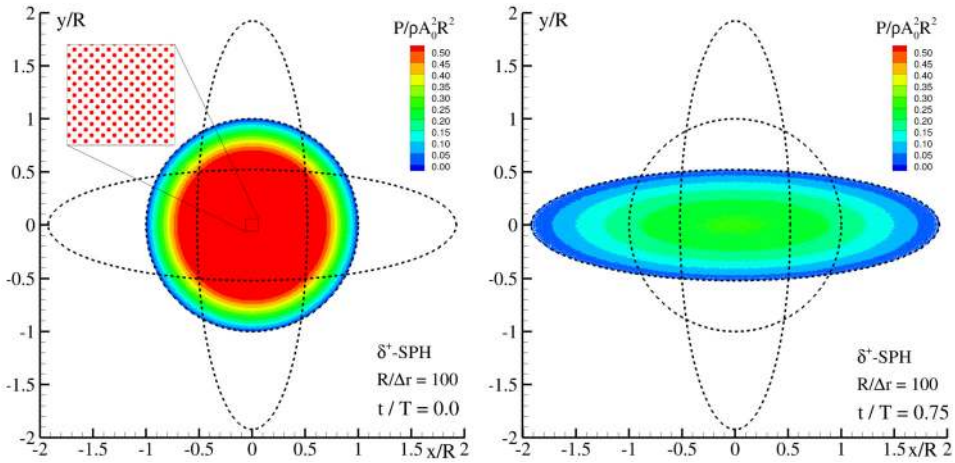

Fig. 26. Elongation of the droplet along the x axis: comparison between the analytical solution and the numerical result of the consistent δ^+-SPH model with the acoustic damper term ($R/\Delta r = 100$).

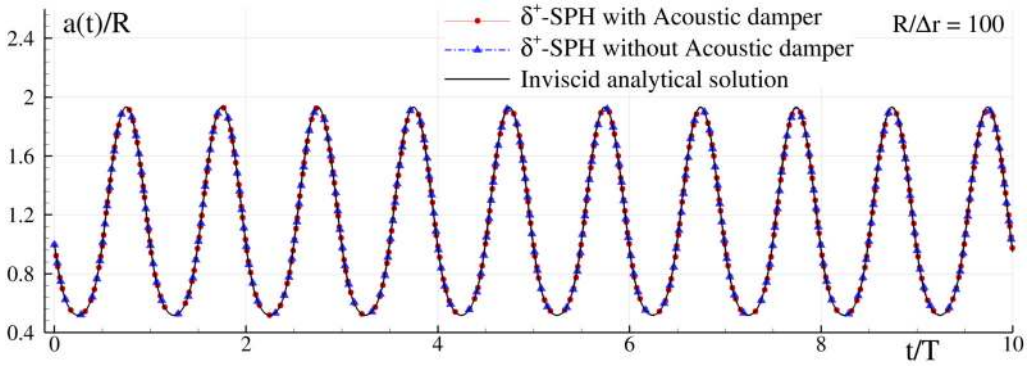

Fig. 27. Time evolution of the elongation of the droplet along the x axis: comparison between the analytical solution (solid line) and the numerical result of the consistent δ^+-SPH model with and without the acoustic damper term. The spatial resolution is $R/\Delta r = 100$.

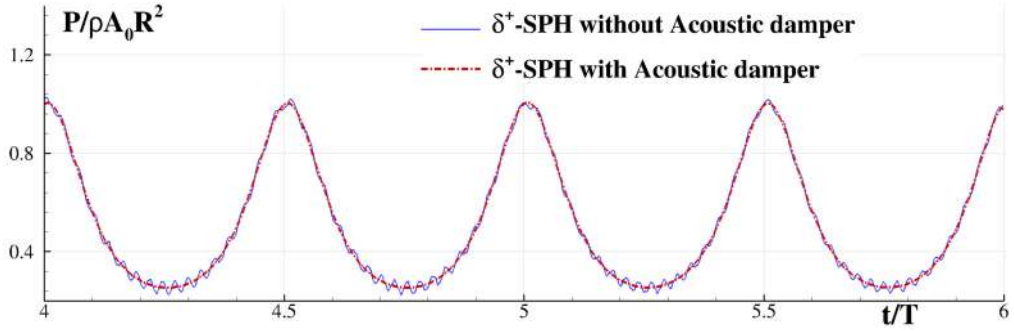

Fig. 28. Time evolution of the pressure at the droplet centre: numerical outputs of the δ^+-SPH with and without using acoustic damper for $R/\Delta r = 100$.

The time history of the droplet elongations along x axis is plotted in Fig. 27 and compared with the results without the acoustic damper term and with the analytical solution. In all the cases a good agreement is observed. In Fig. 28, the numerical solutions for the pressure field at the droplet centre with and without the acoustic damper term are shown for two periods of oscillation. In [49] the occurrence of spurious pressure noise was observed and this led the authors to propose a pressure filtering technique in the post-process. On the contrary, the use of the acoustic damper term considerably reduces this issue as sketched in the Fig. 28.

In Antuono et al. [3] the δ-SPH model was used to carry out a detailed study on the energy conservation properties of that model. Inviscid SPH simulations were run to show that, with advanced SPH schemes (*e.g.* using diffusive terms), the

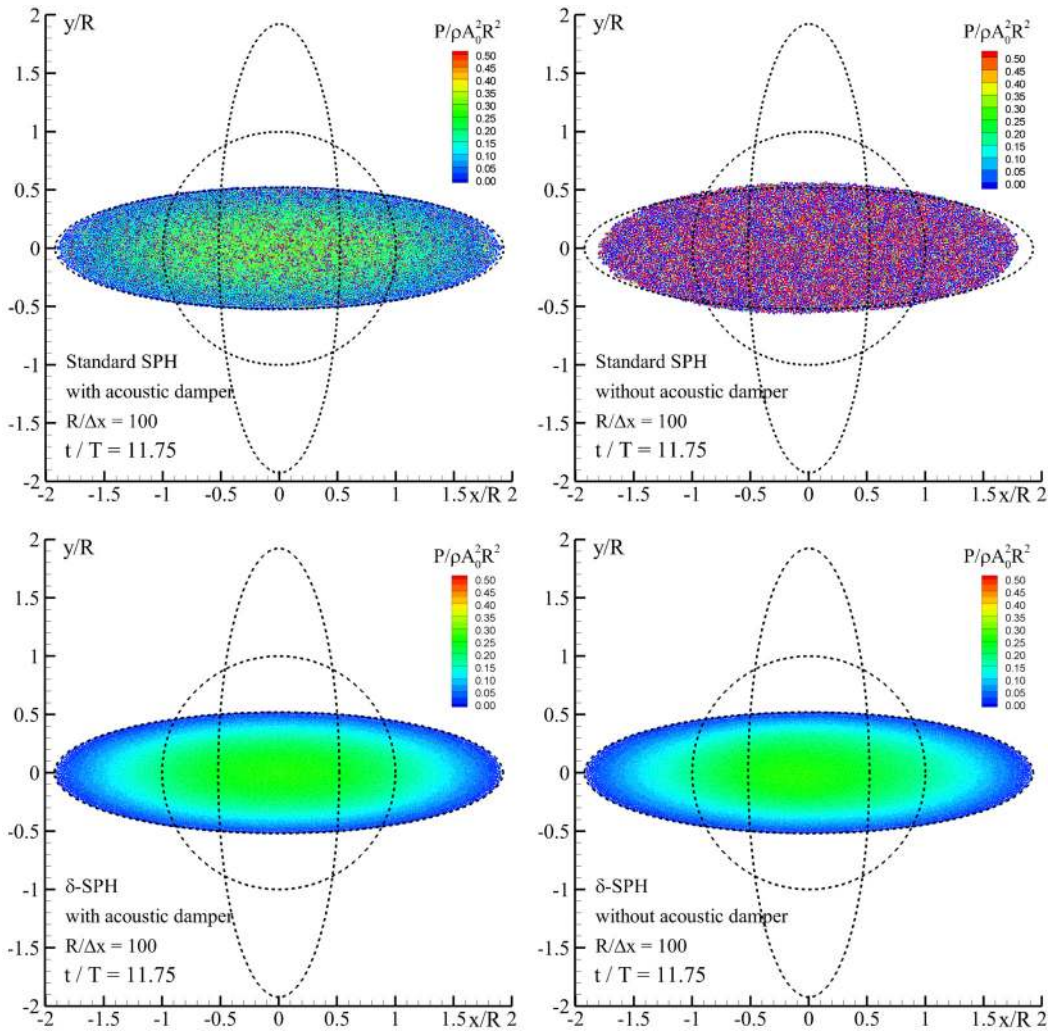

Fig. 29. Elongation of the droplet along the x axis: the pressure field at $t/T = 11.75$ as predicted by the Standard SPH and δ-SPH schemes with (left column) and without (right column) the acoustic damper.

droplet is allowed to oscillate for many periods with small energy dissipation. Antuono et al. [3] also pointed out that in standard SPH simulations (that is, without any diffusive term) a nonphysical accumulation of the inner energy was observed.

In this section, we show that the acoustic damper works as effectively as the density diffusive term to prevent the nonphysical conversion from mechanical energy to internal energy.

Fig. 29 displays a snapshot of the inviscid droplet evolution at $t/T = 11.75$ along with the pressure field as predicted by using the Standard SPH scheme with (left panel) and without (right panel) the acoustic damper. The use of the acoustic damper alone largely improves the simulation and allows for a better conservation of energy. In fact, as shown in Fig. 30, the absence of any sort of diffusion in the standard SPH model leads to a constant increase of the elastic potential energy to the detriment of the total mechanical energy (see Fig. 31).

On the contrary, all the schemes with diffusive terms (*i.e.* the δ-SPH model, the standard SPH with the acoustic damper and the δ^+-SPH with the acoustic damper) provide a good conservation of the elastic potential energy and, consequently, a better conservation of the total mechanical energy in comparison with the standard SPH model.

Incidentally, we observe that the use of the acoustic damper term alone is not enough to remove the small-scale noise from the pressure field (compare, for example, the left plots of Fig. 29). In fact, this benchmark problem is characterized by a small generation of acoustic waves and, consequently, the acoustic damper term is expected to play a minor role on the overall evolution. On the contrary, there is a large production of high-frequency spurious oscillations that are effectively removed by the action of the diffusive term in the continuity equation of the δ-SPH model. This behaviour proves, in fact, a good property of the acoustic damper term, since it confirms that this term mainly acts to reduce the acoustic waves, while it has a minor effect on the remaining components of the pressure field. This latter point is further inspected in the following section.

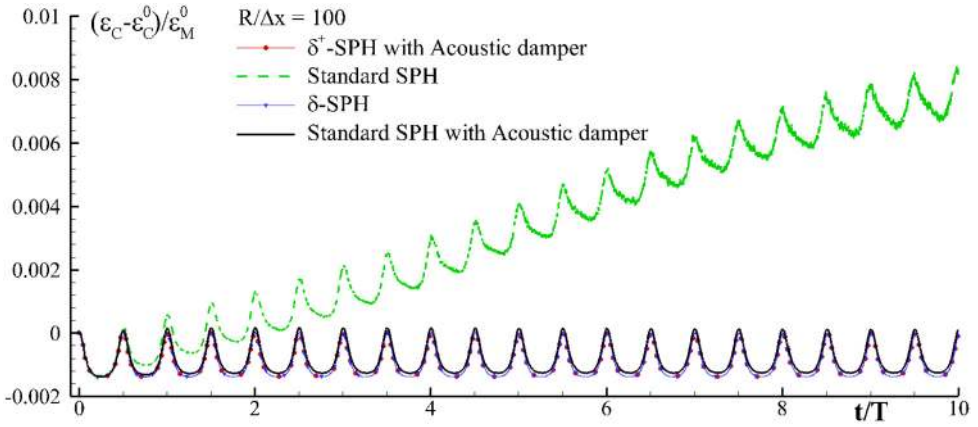

Fig. 30. Time evolution of the elastic potential energy $\mathcal{E}_C$ of the inviscid droplet: comparison between the results of different SPH schemes. The symbol $\mathcal{E}_C^0$ denotes the elastic energy at the initial time.

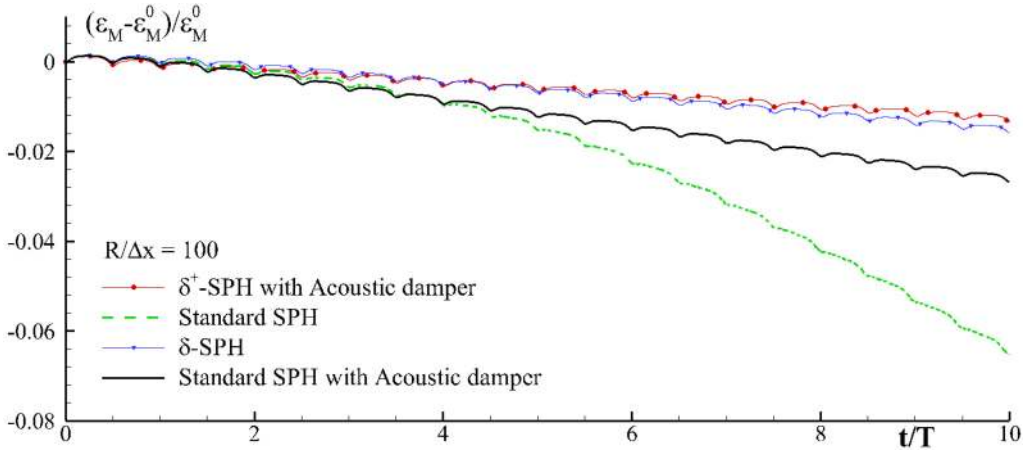

Fig. 31. Time evolution of the total mechanical energy $\mathcal{E}_M$ of the inviscid droplet: comparison between the results of different SPH schemes. The symbol $\mathcal{E}_M^0$ denotes the global mechanical energy at the initial time.

5.2. Shallow-water sloshing

As a second test case, we consider the sloshing motion in shallow-water conditions described in [8]. Specifically, a rectangular tank of length $L = 1$ m and width $D = 0.1$ m is partially filled by water with depth $H = 0.03$ m at rest. Starting from this condition, the tank is moved through an external sinusoidal sway motion with amplitude $A = 0.07$ m and a period $T = 3$ s. A linear ramp is also applied for a time window of 3 periods. Twenty oscillations have been simulated in order to ensure the achievement of a periodic state regime in the sloshing motion. Incidentally, we highlight that the periodic regime has to be intended in a statistical sense, because of the turbulence induced by the breaking bore events inside the tank. The plot of Fig. 32 depicts the time history of the tank centre. This test was firstly simulated in [8] and [64] by using the δ-SPH and the δ^+-SPH models, while in [49] this test-case was used to analyse the influence of the weak-compressibility assumption on the generation of the pressure noise. In this latter work the pressure was filtered in a post-process in order to obtain smooth pressure time signal on the fixed probes. Here, we show that the implementation of the proposed acoustic damper term drastically reduces the acoustic noise and makes the use of the filtering procedure superfluous.

In all the simulations the particle resolution is $H/\Delta r = 50$ and the speed of sound chosen for the numerical simulations is $c = 20\,c_w$ where $c_w = \sqrt{gH}$ is the wave celerity in shallow water conditions.

As pointed out in [8] the friction effects of the viscous boundary layer along the lateral and bottom walls cannot be neglected. On the other hand, the adopted spatial resolution is not fine enough to resolve the thin boundary layer regions. Furthermore, since the simulation is performed in 2D framework we cannot take into account the friction effects of the later walls which have a non-negligible role on the flow, because of the small tank width D. To overcome these limits in

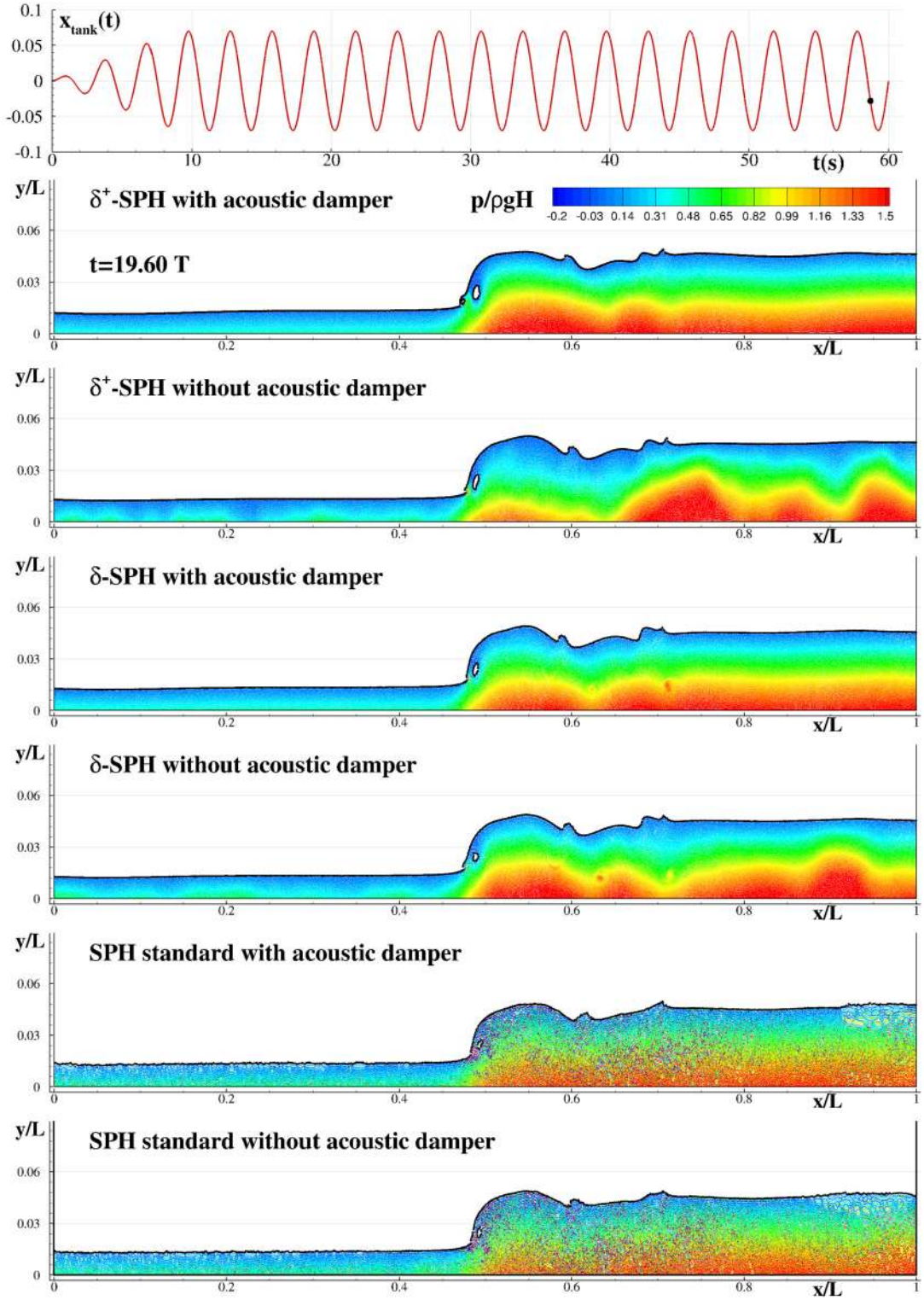

Fig. 32. Snapshots of the pressure field in the shallow-water sloshing flow for different weakly-compressible SPH models with and without the acoustic damper term.

[8] a free-slip boundary condition is enforced on the tank walls and the artificial viscosity of the fluid is tuned through a viscous coefficient β derived by [29]:

$$\alpha = \frac{\beta}{5k^2 c_0 H}\left(\frac{H}{\Delta r}\right), \qquad \beta = 4\nu k^2 + \sqrt{\frac{k c_w \nu}{2}}\left(\frac{2H + D}{H D}\right), \tag{28}$$

where $k = \pi/L$ is the wave number and ν is the kinematic viscosity of the water. In the specific problem under investigation $\beta \simeq 0.049$ and $\alpha \simeq 0.15$.

Fig. 32 displays a snapshot of the fluid evolution and of the pressure field as obtained by using the δ^+-SPH, the δ-SPH and the standard SPH with and without the acoustic damper term. In all the cases, the acoustic damper term completely removes the train of acoustic waves that is generated by the plunging wave front and that travels along the tank. It is however interesting to focus on the bottom panels (*i.e.* those dedicated to the standard SPH simulations). In this case a high-frequency spurious noise is observed in the region close to the right wall and near the overturning plunging wave, regardless of the use of the acoustic damper term. This sort of noise is generated by the nonlinearities of the particle system and is characterized by wavelengths comparable with the kernel radius. Since it is not related to the acoustic of the fluid, it cannot be eliminated by the acoustic damper term. On the contrary, the presence of the diffuse term in the δ^+-SPH and the δ-SPH helps remove this phenomenon. This suggests that the acoustic damper term has not to be regarded as an alternative to the use of the diffusive term in the continuity equation. Conversely, the compound implementation of the acoustic term and of the diffusive term of the δ-SPH proves to be the most effective choice to obtain simulations that are free from any unwanted noise in the pressure field.

6. Conclusions

In the present work an acoustic damper term is proposed to reduce acoustic pressure waves in weakly-compressible SPH schemes. A theoretical framework for this term is given along with an analysis of the energy balance and of the induced rate of dissipation. Furthermore, a practical study on the setting of the time step in numerical simulations is provided when the acoustic damper term is implemented.

A number of both 2D and 3D numerical benchmarks are, then, considered to demonstrate that the proposed term is effective for different weakly-compressible SPH schemes, and that it provides a pressure field that is free from acoustic component. In particular, the use of the acoustic damper term makes the numerical outputs similar to those obtained by using the incompressible variants of the SPH, retaining the advantages of the weakly-compressible models (*i.e.* avoiding the solution of a linear system associated with the Poisson equation for the pressure field). Furthermore, convergence studies prove that, similar to other diffusive terms, the acoustic damper term converges to zero as the particle resolution increases, proving to be numerically consistent.

Finally, the results of Section 5 show that the behaviour of the acoustic damper term is essentially different from the use of a diffusive term in the continuity equation, since the latter primarily dissipates the spurious noise generated at wavelengths comparable with the inter-particle distance.

CRediT authorship contribution statement

P.N. Sun: Funding acquisition, Methodology, Software, Validation. **C. Pilloton:** Visualization, Writing – review & editing. **M. Antuono:** Conceptualization, Funding acquisition, Methodology, Writing – original draft. **A. Colagrossi:** Conceptualization, Funding acquisition, Software, Supervision.

Declaration of competing interest

The authors declare the following financial interests/personal relationships which may be considered as potential competing interests: Andrea Colagrossi reports financial support was provided by Horizon 2020 Europe (Grant No. 815044). Matteo Antuono reports financial support was provided by Government of Italy Ministry of Education University and Research (Grant Agreement No. 20172B7MY9 003). Peng-Nan Sun reports financial support was provided by National Natural Science Foundation of China (Grant Nos. 12002404 & 51679053).

Data availability

Data will be made available on request.

Acknowledgements

The work was partially supported by the SLOWD project which received funding from the European Union's Horizon 2020 research and innovation program under Grant No. 815044 and partially by the FUNBREAK-PRIN2017 project funded by the Italian Ministry MIUR under Grant Agreement No. 20172B7MY9 003. Dr. Peng-Nan Sun is funded by National Natural Science Foundation of China (Grant Nos. 52171329 & 12002404).

References

[1] M. Antuono, A. Colagrossi, S. Marrone, Numerical diffusive terms in weakly-compressible SPH schemes, Comput. Phys. Commun. 183 (12) (2012) 2570–2580.
[2] M. Antuono, A. Colagrossi, S. Marrone, D. Molteni, Free-surface flows solved by means of SPH schemes with numerical diffusive terms, Comput. Phys. Commun. 181 (3) (2010) 532–549.
[3] M. Antuono, S. Marrone, A. Colagrossi, B. Bouscasse, Energy balance in the δ-SPH scheme, Comput. Methods Appl. Mech. Eng. 289 (2015) 209–226.
[4] M. Antuono, S. Marrone, A. Di Mascio, A. Colagrossi, Smoothed particle hydrodynamics method from a large eddy simulation perspective. Generalization to a quasi-Lagrangian model, Phys. Fluids 33 (1) (2021) 015102.
[5] M. Antuono, P.N. Sun, S. Marrone, A. Colagrossi, The δ-ALE-SPH model: an arbitrary Lagrangian-Eulerian framework for the δ-SPH model with particle shifting technique, Comput. Fluids 216 (2021) 104806.
[6] M. Antuono, S. Marrone, A. Colagrossi, Violent wave impacts and loadings using the δ-SPH method, in: Advanced Numerical Modelling of Wave Structure Interactions, CRC Press, 2021, pp. 121–147.
[7] J. Bonet Avalos, M. Antuono, A. Colagrossi, A. Souto-Iglesias, Shear-viscosity-independent bulk-viscosity term in smoothed particle hydrodynamics, Phys. Rev. E 101 (Jan 2020) 013302.
[8] B. Bouscasse, M. Antuono, A. Colagrossi, C. Lugni, Numerical and experimental investigation of nonlinear shallow water sloshing, Int. J. Nonlinear Sci. Numer. Simul. 14 (2) (2013) 123–138.
[9] M. Breuer, D. Hänel, A dual time-stepping method for 3-d, viscous, incompressible vortex flows, Comput. Fluids 22 (4–5) (1993) 467–484.
[10] B. Buchner, Green Water on Ship-type Offshore Structures, PhD thesis, Delft University of Technology, 2002.
[11] X.Y. Cao, F.R. Ming, A. Zhang, Sloshing in a rectangular tank based on SPH simulation, Appl. Ocean Res. 47 (2014) 241–254.
[12] J.L. Cercos-Pita, M. Antuono, A. Colagrossi, A. Souto-Iglesias, SPH energy conservation for fluid–solid interactions, Comput. Methods Appl. Mech. Eng. 317 (2017) 771–791.
[13] A. Colagrossi, M. Antuono, A. Souto-Iglesias, D. Le Touzé, Theoretical analysis and numerical verification of the consistency of viscous smoothed-particle-hydrodynamics formulations in simulating free-surface flows, Phys. Rev. E 84 (2011) 026705.
[14] A. Colagrossi, D. Durante, J. Bonet Avalos, A. Souto-Iglesias, Discussion of Stokes' hypothesis through the smoothed particle hydrodynamics model, Phys. Rev. E 96 (August 2017) 023101.
[15] A. Colagrossi, M. Landrini, Numerical simulation of interfacial flows by smoothed particle hydrodynamics, J. Comput. Phys. 191 (2003) 448–475.
[16] M.J. Cooker, Liquid impact, kinetic energy loss and compressibility: Lagrangian, Eulerian and acoustic viewpoints, J. Eng. Math. 44 (3) (2002) 259–276.
[17] W. Dehnen, H. Aly, Improving convergence in smoothed particle hydrodynamics simulations without pairing instability, Mon. Not. R. Astron. Soc. 425 (2) (2012) 1068–1082.
[18] J.M. Domínguez, G. Fourtakas, C. Altomare, R.B. Canelas, A. Tafuni, O. García-Feal, I. Martínez-Estévez, A. Mokos, R. Vacondio, A.J.C. Crespo, et al., Dualsphysics: from fluid dynamics to multiphysics problems, Comput. Part. Mech. (2021) 1–29.
[19] D. Durante, O. Giannopoulou, A. Colagrossi, Regimes identification of the viscous flow past an elliptic cylinder for Reynolds number up to 10000, Commun. Nonlinear Sci. Numer. Simul. 102 (2021) 105902.
[20] P. Español, M. Revenga, Smoothed dissipative particle dynamics, Phys. Rev. E 67 (2) (Feb 2003) 026705.
[21] I. Federico, S. Marrone, A. Colagrossi, F. Aristodemo, M. Antuono, Simulating 2D open-channel flows through an SPH model, Eur. J. Mech. B, Fluids 34 (2012) 35–46.
[22] A. Ferrari, M. Dumbser, E.F. Toro, A. Armanini, A new 3D parallel SPH scheme for free surface flows, Comput. Fluids 38 (6) (2009) 1203–1217.
[23] A. Ghavamian, C.H. Lee, A.J. Gil, J. Bonet, T. Heuzé, L. Stainier, An entropy-stable smooth particle hydrodynamics algorithm for large strain thermo-elasticity, Comput. Methods Appl. Mech. Eng. 379 (2021) 113736.
[24] O. Giannopoulou, A. Colagrossi, A. Di Mascio, C. Mascia, Chorin's approaches revisited: vortex particle method vs finite volume method, Eng. Anal. Bound. Elem. 106 (2019) 371–388.
[25] K. Gong, H. Liu, B.L. Wang, Water entry of a wedge based on SPH model with an improved boundary treatment, J. Hydrodyn. 21 (6) (2009) 750–757.
[26] M.D. Green, J. Peiró, Long duration SPH simulations of sloshing in tanks with a low fill ratio and high stretching, Comput. Fluids 174 (2018) 179–199.
[27] M.D. Green, R. Vacondio, J. Peiró, A smoothed particle hydrodynamics numerical scheme with a consistent diffusion term for the continuity equation, Comput. Fluids 179 (2019) 632–644.
[28] C. Hermange, G. Oger, Y. Le Chenadec, D. Le Touzé, A 3D SPH–FE coupling for FSI problems and its application to tire hydroplaning simulations on rough ground, Comput. Methods Appl. Mech. Eng. 355 (2019) 558–590.
[29] G.H. Keulegan, Energy dissipation in standing waves in rectangular basins, J. Fluid Mech. 6 (1) (1959) 33–50.
[30] A. Khayyer, H. Gotoh, S.D. Shao, Corrected incompressible SPH method for accurate water-surface tracking in breaking waves, Coast. Eng. 55 (3) (2008) 236–250.
[31] A. Khayyer, H. Gotoh, Y. Shimizu, Comparative study on accuracy and conservation properties of two particle regularization schemes and proposal of an optimized particle shifting scheme in ISPH context, J. Comput. Phys. 332 (2017) 236–256.
[32] K.M.T. Kleefsman, G. Fekken, A.E.P. Veldman, B. Iwanowski, B. Buchner, A volume-of-fluid based simulation method for wave impact problems, J. Comput. Phys. 206 (1) (6/10 2005) 363–393.
[33] S.I. Inutsuka, Reformulation of smoothed particle hydrodynamics with Riemann solver, J. Comput. Phys. 179 (1) (2002) 238–267.
[34] M. Lastiwka, M. Basa, N.J. Quinlan, Permeable and non-reflecting boundary conditions in SPH, Int. J. Numer. Methods Fluids 61 (7) (2008) 709–724.
[35] E.S. Lee, C. Moulinec, R. Xu, D. Violeau, D. Laurence, P. Stansby, Comparisons of weakly compressible and truly incompressible algorithms for the SPH mesh free particle method, J. Comput. Phys. 227 (18) (2008) 8417–8436.
[36] E.S. Lee, D. Violeau, R. Issa, S. Ploix, Application of weakly compressible and truly incompressible SPH to 3-d water collapse in waterworks, J. Hydraul. Res. 48 (sup1) (2010) 50–60.
[37] C. Liang, A. Chan, X. Liu, A. Jameson, An artificial compressibility method for the spectral difference solution of unsteady incompressible Navier-Stokes equations on multiple grids, in: 49th AIAA Aerospace Sciences Meeting Including the New Horizons Forum and Aerospace Exposition, 2011, p. 48.
[38] E.Y. Lo, S. Shao, Simulation of near-shore solitary wave mechanics by an incompressible SPH method, Appl. Ocean Res. 24 (5) (2002) 275–286.
[39] L. Lobovský, E. Botia-Vera, F. Castellana, J. Mas-Soler, A. Souto-Iglesias, Experimental investigation of dynamic pressure loads during dam break, J. Fluids Struct. 48 (2014) 407–434.
[40] M. Luo, A. Khayyer, P. Lin, Particle methods in ocean and coastal engineering, Appl. Ocean Res. 114 (2021) 102734.
[41] A. Madsen, H.A. Schäffer, A discussion of artificial compressibility, Coast. Eng. 53 (1) (2006) 93–98.
[42] S. Marrone, M. Antuono, A. Colagrossi, G. Colicchio, D. Le Touzé, G. Graziani, δ-SPH model for simulating violent impact flows, Comput. Methods Appl. Mech. Eng. 200 (13–16) (2011) 1526–1542.
[43] S. Marrone, A. Colagrossi, M. Antuono, G. Colicchio, G. Graziani, An accurate SPH modeling of viscous flows around bodies at low and moderate Reynolds numbers, J. Comput. Phys. 245 (2013) 456–475.
[44] S. Marrone, A. Colagrossi, M. Antuono, C. Lugni, M.P. Tulin, A 2D+t SPH model to study the breaking wave pattern generated by fast ships, J. Fluids Struct. 27 (8) (2011) 1199–1215.

[45] S. Marrone, A. Colagrossi, A. Di Mascio, D. Le Touzé, Prediction of energy losses in water impacts using incompressible and weakly compressible models, J. Fluids Struct. 54 (2015) 802–822.
[46] S. Marrone, A. Colagrossi, A. Di Mascio, D. Le Touzé, Analysis of free-surface flows through energy considerations: single-phase versus two-phase modeling, Phys. Rev. E 93 (May 2016) 053113.
[47] S. Marrone, A. Colagrossi, D. Le Touzé, G. Graziani, Fast free-surface detection and level-set function definition in SPH solvers, J. Comput. Phys. 229 (10) (2010) 3652–3663.
[48] Z.F. Meng, A.M. Zhang, J.L. Yan, P.P. Wang, A. Khayyer, A hydroelastic fluid–structure interaction solver based on the Riemann-sph method, Comput. Methods Appl. Mech. Eng. 390 (2022) 114522.
[49] D.D. Meringolo, A. Colagrossi, S. Marrone, F. Aristodemo, On the filtering of acoustic components in weakly-compressible SPH simulations, J. Fluids Struct. 70 (2017) 1–23.
[50] D.D. Meringolo, S. Marrone, A. Colagrossi, Y. Liu, A dynamic δ-SPH model: how to get rid of diffusive parameter tuning, Comput. Fluids 179 (2019) 334–355.
[51] J. Michel, D. Durante, A. Colagrossi, S. Marrone, Energy dissipation in violent three dimensional sloshing flows induced by high-frequency vertical accelerations, Phys. Fluids 34 (2022) 102114.
[52] J.J. Monaghan, SPH without a tensile instability, J. Comput. Phys. 159 (2) (2000) 290–311.
[53] J.J. Monaghan, Smoothed particle hydrodynamics, Rep. Prog. Phys. 68 (8) (2005) 1703.
[54] J.J. Monaghan, R.A. Gingold, Shock simulation by the particle method SPH, J. Comput. Phys. 52 (2) (1983) 374–389.
[55] J.J. Monaghan, A. Rafiee, A simple SPH algorithm for multi-fluid flow with high density ratios, Int. J. Numer. Methods Fluids 71 (5) (2013) 537–561.
[56] C.-D. Munz, S. Roller, R. Klein, K.J. Geratz, The extension of incompressible flow solvers to the weakly compressible regime, Comput. Fluids 32 (2) (2003) 173–196.
[57] A.-N. Parshikov, A. Stanislav, Smoothed particle hydrodynamics using interparticle contact algorithms, J. Comput. Phys. 180 (1) (2002) 358–382.
[58] P. Rastelli, R. Vacondio, J.C. Marongiu, G. Fourtakas, B.D. Rogers, Implicit iterative particle shifting for meshless numerical schemes using kernel basis functions, Comput. Methods Appl. Mech. Eng. 393 (2022) 114716.
[59] E. Rossi, A. Colagrossi, B. Bouscasse, G. Graziani, The diffused vortex hydrodynamics method, Commun. Comput. Phys. 18 (2) (2015) 351–379.
[60] E. Rossi, D. Durante, S. Marrone, A. Colagrossi, A novel multi-resolution technique for solving complex vorticity patterns in planar viscous flows past bodies through the dvh method, Comput. Methods Appl. Mech. Eng. 396 (2022) 115082.
[61] J.H. Seo, Y.J. Moon, Linearized perturbed compressible equations for low Mach number aeroacoustics, J. Comput. Phys. 218 (2) (2006) 702–719.
[62] M.S. Shadloo, G. Oger, D. Le Touzé, Smoothed particle hydrodynamics method for fluid flows, towards industrial applications: motivations, current state, and challenges, Comput. Fluids 136 (2016) 11–34.
[63] P.N. Sun, A. Colagrossi, S. Marrone, M. Antuono, A. Zhang, Multi-resolution Delta-plus-SPH with tensile instability control: towards high Reynolds number flows, Comput. Phys. Commun. 224 (2018) 63–80.
[64] P.N. Sun, A. Colagrossi, S. Marrone, M. Antuono, A. Zhang, A consistent approach to particle shifting in the δ-Plus-SPH model, Comput. Methods Appl. Mech. Eng. 348 (2019) 912–934.
[65] P.N. Sun, D. Le Touzé, G. Oger, A. Zhang, An accurate FSI-SPH modeling of challenging fluid-structure interaction problems in two and three dimensions, Ocean Eng. 221 (2021) 108552.
[66] P.N. Sun, D. Le Touzé, A. Zhang, Study of a complex fluid-structure dam-breaking benchmark problem using a multi-phase SPH method with APR, Eng. Anal. Bound. Elem. 104 (2019) 240–258.
[67] P.N. Sun, F. Ming, A. Zhang, Numerical simulation of interactions between free surface and rigid body using a robust SPH method, Ocean Eng. 98 (2015) 32–49.
[68] P.N. Sun, A. Zhang, S. Marrone, F. Ming, An accurate and efficient SPH modeling of the water entry of circular cylinders, Appl. Ocean Res. 72 (2018) 60–75.
[69] P.N. Sun, C. Pilloton, M. Antuono, A. Colagrossi, Weakly-compressible SPH schemes with an acoustic-damper term, in: Proceedings of the 16 th SPHERIC International Workshop, Catania, 6–9 June 2022.
[70] J.W. Swegle, D.L. Hicks, S.W. Attaway, Smoothed particle hydrodynamics stability analysis, J. Comput. Phys. 116 (1995) 123–134.
[71] J.P. Vila, On particle weighted methods and smooth particle hydrodynamics, Math. Models Methods Appl. Sci. 9 (02) (1999) 161–209.
[72] J. Von Neumann, R.D. Ritchtmyer, A new method for the numerical calculation of hydrodynamics shocks, J. Appl. Phys. 21 (1950) 232–247.
[73] J. Wang, C. Lugni, O.M. Faltinsen, Experimental and numerical investigation of a freefall wedge vertically entering the water surface, Appl. Ocean Res. 51 (2015) 181–203.
[74] H. Wendland, Piecewise polynomial, positive definite and compactly supported radial functions of minimal degree, Adv. Comput. Math. 4 (4) (1995) 389–396.
[75] T. Ye, D. Pan, C. Huang, M. Liu, Smoothed particle hydrodynamics (SPH) for complex fluid flows: recent developments in methodology and applications, Phys. Fluids 31 (1) (2019) 011301.
[76] C. Zhang, Y. Zhu, Y. Yu, D. Wu, M. Rezavand, S. Shao, X. Hu, An artificial damping method for total Lagrangian sph method with application in biomechanics, Eng. Anal. Bound. Elem. 143 (2022) 1–13.
[77] S. Lind, R. Xu, P. Stansby, B. Rogers, Incompressible smoothed particle hydrodynamics for free-surface flows: a generalised diffusion-based algorithm for stability and validations for impulsive flows and propagating waves, J. Comput. Phys. 231 (2012) 1499–1523.
[78] J. Dominguez, G. Fourtakas, C. Altomare, R. Canelas, A. Tafuni, O. Garcia-Feal, I. Martinez-Estevez, A. Mokos, R. Vacondio, A. Crespo, et al., DualSPHysics: from fluid dynamics to multiphysics problems, Comput. Part. Mech. 9 (2022) 867–895.
[79] I. Martinez-Estevez, J. Dominguez, B. Tagliafierro, R. Canelas, O. Garcia-Feal, A. Crespo, M. Gomes-Gesteira, Coupling of an SPH-based solver with a multiphysics library, Comput. Phys. Commun. 283 (2023) 108581.
[80] Y. Shimizu, H. Gotoh, A. Khayyer, K. Kita, Fundamental investigation on the applicability of a higher-order consistent ISPH method, Int. J. Offshore Polar Eng. 32 (2022) 275–284.
[81] Y. Peng, A. Zhang, F. Ming, A 3D meshfree crack propagation algorithm for the dynamic fracture in arbitrary curved shell, Comput. Methods Appl. Mech. Eng. 367 (2020) 113139.
[82] M. Lastiwka, M. Basa, N. Quinlan, Permeable and non-reflecting boundary conditions in SPH, Int. J. Numer. Methods Fluids 61 (2009) 709–724.
[83] P. Negi, P. Ramachandran, A. Haftu, An improved non-reflecting outlet boundary condition for weakly-compressible SPH, Comput. Methods Appl. Mech. Eng. 367 (2020) 113119.
[84] G. Oger, D. Le Touzé, D. Guibert, M. De Leffe, J. Biddiscombe, J. Soumagne, J. Piccinali, On distributed memory MPI-based parallelization of SPH codes in massive HPC context, Comput. Phys. Commun. 200 (2016) 1–14.
[85] Z. Ji, F. Xu, A. Takahashi, Y. Sun, Large scale water entry simulation with smoothed particle hydrodynamics on single- and multi-GPU systems, Comput. Phys. Commun. 209 (2016) 1–12.
[86] J. Dominguez, A. Crespo, D. Valdez-Balderas, B. Rogers, M. Gomez-Gesteira, New multi-GPU implementation for smoothed particle hydrodynamics on heterogeneous clusters, Comput. Phys. Commun. 184 (2013) 1848–1860.